

Photospheric Injection of Magnetic Helicity: Connectivity–based Flux Density Method

K. Dalmasse · E. Pariat · P. Démoulin ·
G. Aulanier ·

© Springer ●●●

Abstract Magnetic helicity quantifies how globally sheared and/or twisted is the magnetic field in a volume. This quantity is believed to play a key role in solar activity due to its conservation property. Helicity is continuously injected into the corona during the evolution of active regions (ARs). To better understand and quantify the role of magnetic helicity in solar activity, the distribution of magnetic helicity flux in ARs needs to be studied. The helicity distribution can be computed from the temporal evolution of photospheric magnetograms of ARs such as the ones provided by SDO/HMI and Hinode/SOT. Most recent analyses of photospheric helicity flux derive an helicity flux density proxy based on the relative rotation rate of photospheric magnetic footpoints. Although this proxy allows a good estimate of the photospheric helicity flux, it is still not a true helicity flux density because it does not take into account the connectivity of the magnetic field lines. For the first time, we implement a helicity density which takes into account such connectivity. In order to use it for future observational studies, we test the method and its precision on several types of models involving different patterns of helicity injection. We also test it on more complex configurations — from magnetohydrodynamics (MHD) simulations — containing quasi–separatrix layers. We demonstrate that this connectivity–based helicity flux density proxy is the best to map the true distribution of photospheric helicity injection.

Keywords: Helicity, Magnetic; Helicity, Theory; Magnetic fields, Corona; Active Regions

1. Introduction

Magnetic helicity plays a key role in solar MHD because it is quasi conserved on timescales much smaller than the global energy diffusion timescale (Berger, 1984, 2003). This conservation property constrains the evolution of the magnetic field. In particular, an isolated magnetic field structure with a non-null helicity cannot

LESIA, Observatoire de Paris, CNRS, UPMC, Université
Paris-Diderot, 92195 Meudon, France email:
kevin.dalmasse@obspm.fr

relax to a potential field, even through resistive mechanisms: its minimum energy is theoretically and experimentally bounded by a linear force-free field rather than the potential one (Taylor, 1974; Yamada, 1999). Linton and Antiochos (2002, 2005) have shown that helicity can be used to predict which type of interaction can occur between reconnected flux tubes.

In order for a system to reach the lowest possible energy state, its helicity must be eventually carried away or annihilated. In the solar corona, important helicity carriers are the twisted magnetic structures associated with coronal mass ejections (CMEs) and magnetic clouds. Rust (1994) and Low (1997) have therefore hypothesized that CMEs could be the result of the global conservation of helicity within the solar atmosphere (see also Zhang, Flyer, and Low, 2006, 2012; Zhang and Flyer, 2008). CMEs can transport the large amount of helicity present in ARs that have been injected from the solar interior (van Driel-Gesztelyi *et al.*, 1999; DeVore, 2000; Démoulin *et al.*, 2002; Green *et al.*, 2002a, 2002b; Mandrini *et al.*, 2004; Georgoulis *et al.*, 2009; Kazachenko *et al.*, 2012).

Another possible way for a magnetic system to get its helicity content reduced is through annihilation by magnetic reconnection with other systems containing helicity of a different sign. Through these reconnections, the global system would present a lower absolute amount of magnetic helicity and thus the minimum energy state that could be reached would be also lower. It has thus been conjectured that reconnection between systems of opposite magnetic helicity would lead to a higher energy release (Kusano, Suzuki, and Nishikawa, 1995). Linton, Dahlburg, and Antiochos (2001) have shown that reconnection between two twisted flux tubes is more violent and that more energy is released when the flux tubes have opposite helicity rather than the same sign. Models of flares involving opposite sign of helicity have thus been developed (Kusano *et al.*, 2002, 2004a) and observational studies aiming at detecting ARs with opposite helicity signs have been carried over (Chandra *et al.*, 2010; Romano *et al.*, 2011; Romano and Zuccarello, 2011).

Estimation of the magnetic helicity in the solar atmosphere is not straightforward (see reviews by Démoulin, 2007; Démoulin and Pariat, 2009). The sign of magnetic helicity can be derived from the observation of twisted or sheared structures such as filaments fibrils and barbs, sunspot whorls, magnetic tongues.

A first way to quantitatively determine magnetic helicity is based on magnetic field extrapolations (*e.g.*, Berger, 2003; Démoulin, 2007; Valori, Démoulin, and Pariat, 2012; Jing *et al.*, 2012). Another method to estimate the magnetic helicity has relied on the measurements of its flux through the solar surface (Chae, 2001; Chae, Moon, and Park, 2004). Magnetic helicity fluxes can directly be estimated using sequences of longitudinal magnetograms (Démoulin and Berger, 2003), with improved measurements obtained when full vector magnetograms at high enough cadence are available (Schuck, 2008; Yang and Zhang, 2012). The estimation of the helicity flux has allowed to track the evolution of the helicity injected in many ARs (*e.g.*, Nindos, Zhang, and Zhang, 2003; Yamamoto *et al.*, 2005; Jeong and Chae, 2007; LaBonte, Georgoulis, and Rust, 2007, Yang and Zhang, 2012).

In all studied ARs, an extremely mixed pattern of helicity injection is observed (*e.g.*, Chae, Moon, and Park, 2004; Yamamoto *et al.*, 2005). However Pariat,

Démoulin, and Berger (2005) showed that the analyzed quantity, G_A , was not a proper helicity flux density and that it produced important spurious non-physical signals. They showed that helicity flux density is inherently not a local quantity per unit surface. The physically meaningful helicity flux density is the helicity per elementary flux tube. They proposed two quantities named G_θ and G_Φ (see their derivation in Section 2.2) that can be used as proxies of the helicity flux density through the photosphere.

The first proxy, G_θ , could be directly applied from time sequence of magnetograms (see Chae, 2007; Yang and Zhang, 2012; for improved high-efficient methods to compute G_θ). This proxy, removing the spurious signal of G_A , showed that the helicity flux injection pattern in AR was rather uniform in sign (Pariat *et al.*, 2006). Most ARs do not present important traces of injection of helicity of opposite sign. However, G_θ is not completely free of spurious signal (Pariat, Démoulin, and Berger, 2005, 2006, 2007) and direct interpretations of the maps should be taken with caution.

The second proxy, G_Φ , is the proxy that allows the more truthful representation of the helicity flux distribution. It however requires the knowledge of the magnetic field connectivity. It has so far never been directly used with any observed data. Its implementation is indeed not straightforward in non-analytical fields as it requires a good knowledge of the 3D magnetic field. As 3D magnetic field extrapolations would become more common and hopefully more reliable, it will be more easy to use G_Φ on observational cases.

The present study is a first step toward implementing a method that would be used with observed data (*i.e.*, magnetic field extrapolations). The aim is to practically test the G_Φ method on simplified solar configurations in order to determine typical patterns of G_Φ . This would help to later interpret observed G_Φ maps. It will also help us to understand the limit and precision of the method.

The manuscript is organized as follows: Section 2 presents the analytical derivation of G_θ and G_Φ and summarizes some of the expected properties. In Section 3, we present the method and introduce the different magnetic configurations and flow patterns studied. Next, we present the results of our analyzes on different models: first on two analytical configurations (Sections 4 and 5), then on magnetic extrapolations (Section 6), and finally on MHD simulations with complex connectivities (Section 7). We conclude in Section 8.

2. Photospheric Helicity Flux

2.1. Magnetic Helicity Flux

Let \mathcal{V} be a magnetic volume bounded by a surface \mathcal{S} , with magnetic flux crossing \mathcal{S} (*e.g.*, \mathcal{V} is part of the corona). A gauge invariant relative magnetic helicity, H , can be written as follows (Finn and Antonsen, 1985):

$$H = \int_{\mathcal{V}} (\mathbf{A} + \mathbf{A}_p) \cdot (\mathbf{B} - \mathbf{B}_p) \, d^3x, \quad (1)$$

where \mathbf{A} is the vector potential ($\mathbf{B} = \nabla \times \mathbf{A}$). In this formula, the magnetic helicity is defined relatively to the potential magnetic field, \mathbf{B}_p ($\mathbf{B}_p = \nabla \times \mathbf{A}_p$), that has the same normal component (B_n) on \mathcal{S} as \mathbf{B} .

Pariat, Démoulin, and Berger (2005) demonstrated that the magnetic helicity flux across \mathcal{S} could be written as the summation of the relative rotation rate, on \mathcal{S} , of all pairs of elementary magnetic flux tubes weighted by their magnetic flux:

$$\frac{dH}{dt} = -\frac{1}{2\pi} \int_{\mathcal{S}} \int_{\mathcal{S}'} \frac{d\theta(\mathbf{x} - \mathbf{x}')}{dt} B_n(\mathbf{x}) B_n(\mathbf{x}') d\mathcal{S} d\mathcal{S}', \quad (2)$$

where

$$\frac{d\theta(\mathbf{x} - \mathbf{x}')}{dt} = \frac{((\mathbf{x} - \mathbf{x}') \times (\mathbf{u} - \mathbf{u}')) \cdot \mathbf{n}}{|\mathbf{x} - \mathbf{x}'|^2} \quad (3)$$

is the relative rotation rate between the two photospheric points \mathbf{x} and \mathbf{x}' moving on the photosphere with the flux transport velocity \mathbf{u} and \mathbf{u}' respectively.

Observationally, a time series of magnetograms provides B_n at the photosphere. Several methods have been developed to estimate \mathbf{u} . One is based on tracking the photospheric spatial evolution of magnetic flux tubes from magnetograms and is called Local Correlation Tracking (LCT; Chae (2001) and references therein). Others are based on solving the induction equation using magnetograms (Longcope, 2004). There are also methods that solve the induction equation in the spirit of the LCT method (Welsch *et al.*, 2004, 2007; Schuck, 2005, 2006, 2008).

2.2. Magnetic Helicity Flux Density

From Equation (2), Pariat, Démoulin, and Berger (2005) defined a new helicity flux density proxy, G_θ , that represents the distribution of helicity density at the photosphere:

$$G_\theta(\mathbf{x}) = -\frac{B_n}{2\pi} \int_{\mathcal{S}'} \frac{d\theta(\mathbf{x} - \mathbf{x}')}{dt} B'_n d\mathcal{S}'. \quad (4)$$

However, magnetic helicity is a global quantity. The helicity density and the density of helicity flux are only meaningful when considering a whole magnetic flux tube, which requires the knowledge of the magnetic connectivity in the volume \mathcal{V} (Pariat, Démoulin, and Berger, 2005).

Separating Equation (2) into two terms, *i.e.*, the flux of helicity due to the relative rotation of positive and negative polarities — first term of Equation (5) — and the one due to the relative rotation of each polarity — second term of Equation (5), they rewrite Equation (2) as follows:

$$\begin{aligned} \frac{dH}{dt} &= \frac{1}{2\pi} \int \int_{B_n \cdot B'_n < 0} \frac{d\theta}{dt} |B_n B'_n| d\mathcal{S} d\mathcal{S}' \\ &\quad - \frac{1}{2\pi} \int \int_{B_n \cdot B'_n > 0} \frac{d\theta}{dt} B_n B'_n d\mathcal{S} d\mathcal{S}'. \end{aligned} \quad (5)$$

Using $d\Phi_+ = B_n(\mathbf{x}_+) d\mathcal{S}$ and $d\Phi_- = -B_n(\mathbf{x}_-) d\mathcal{S}$ the elementary magnetic fluxes in the positive and negative polarity respectively, Equation (5) leads to:

$$\begin{aligned} \frac{dH}{dt} &= \frac{1}{2\pi} \int_{\Phi_+} \int_{\Phi'_-} \frac{d\theta(\mathbf{x}_+ - \mathbf{x}'_-)}{dt} d\Phi_+ d\Phi'_- \\ &+ \frac{1}{2\pi} \int_{\Phi_-} \int_{\Phi'_+} \frac{d\theta(\mathbf{x}_- - \mathbf{x}'_+)}{dt} d\Phi_- d\Phi'_+ \\ &- \frac{1}{2\pi} \int_{\Phi_+} \int_{\Phi'_+} \frac{d\theta(\mathbf{x}_+ - \mathbf{x}'_+)}{dt} d\Phi_+ d\Phi'_+ \\ &- \frac{1}{2\pi} \int_{\Phi_-} \int_{\Phi'_-} \frac{d\theta(\mathbf{x}_- - \mathbf{x}'_-)}{dt} d\Phi_- d\Phi'_-. \end{aligned} \quad (6)$$

Since the magnetic flux is conserved along the flux tubes, we have $d\Phi_+ = d\Phi_-$ and $d\Phi'_+ = d\Phi'_-$. Then, by considering two generic magnetic field lines “ a ” and “ c ” respectively going from footpoint \mathbf{x}_{a+} to \mathbf{x}_{a-} and from \mathbf{x}_{c+} to \mathbf{x}_{c-} (Figure 1a), and by regrouping all four terms of Equation (6), we can rewrite the helicity flux by explicitly including the field lines connectivity in \mathcal{V} :

$$\frac{dH}{dt} = \int_{\Phi} \left. \frac{dh_{\Phi}}{dt} \right|_c d\Phi_{c+}, \quad (7)$$

$$\text{with } \left. \frac{dh_{\Phi}}{dt} \right|_c = \frac{1}{2\pi} \int_{\Phi} \left(\frac{d\theta(\mathbf{x}_{c+} - \mathbf{x}_{a-})}{dt} + \frac{d\theta(\mathbf{x}_{c-} - \mathbf{x}_{a+})}{dt} - \frac{d\theta(\mathbf{x}_{c+} - \mathbf{x}_{a+})}{dt} - \frac{d\theta(\mathbf{x}_{c-} - \mathbf{x}_{a-})}{dt} \right) d\Phi_{a+}. \quad (8)$$

In Equation (7), the total helicity flux is now written as the integral over the total magnetic flux crossing \mathcal{S} of the helicity flux density in each elementary flux tube “ c ” that compose \mathcal{V} . Then, by separating the contributions of helicity flux at \mathbf{x}_{c+} from those at \mathbf{x}_{c-} , Pariat, Démoulin, and Berger (2005) expressed the helicity flux density per unit of magnetic flux tube, dh_{Φ}/dt , as a field-weighted average of the flux per unit surface, G_{θ} , at both footpoints \mathbf{x}_{c+} and \mathbf{x}_{c-} of flux tube “ c ”:

$$\left. \frac{dh_{\Phi}}{dt} \right|_c = \frac{G_{\theta}(\mathbf{x}_{c+})}{|B_n(\mathbf{x}_{c+})|} + \frac{G_{\theta}(\mathbf{x}_{c-})}{|B_n(\mathbf{x}_{c-})|}. \quad (9)$$

From Equation (9), a helicity flux density per unit surface can be defined by redistributing the total helicity injected into flux tube “ c ” at both footpoints of the flux tube with the fractions $f(\mathbf{x}_{c+}) = f_+ = f$ and $f(\mathbf{x}_{c-}) = f_- = 1 - f$. They thus defined the best surface helicity flux density proxy, G_{Φ} , by equally sharing dh_{Φ}/dt between the two footpoints of flux tube “ c ”:

$$G_{\Phi}(\mathbf{x}_{c_{\pm}}) = f_{\pm} \left(G_{\theta}(\mathbf{x}_{c_{\pm}}) + \left| \frac{B_n(\mathbf{x}_{c_{\pm}})}{B_n(\mathbf{x}_{c_{\mp}})} \right| G_{\theta}(\mathbf{x}_{c_{\mp}}) \right), \quad (10)$$

with $f_+ = f_- = 1/2$.

There is therefore a conceptual difference between G_θ and G_Φ . The proxy G_Φ assumes that the footpoints of the elementary flux tubes have a knowledge of the helicity injection at the other footpoint. Therefore, when using G_Φ one assumes that the helicity injection process is done with a characteristic timescale which is much larger than the transit time of information within the field line. As such information will be transferred through Alfvénic waves along the field line, G_Φ is meaningful for any process which velocity is smaller than the averaged Alfvén speed along the field line. In the solar atmosphere such condition is easily satisfied as the typical velocities in the photosphere ($< 1 \text{ km s}^{-1}$) are orders of magnitude smaller than the coronal Alfvén speed ($\approx 10^3 - 10^4 \text{ km s}^{-1}$). The different motions that enable the energy storage in the coronal field are consistent with the use of G_Φ . However when considering processes occurring over the Alfvénic timescale, such as magnetic reconnection, this condition may not be fulfilled.

3. Methodology

For the first time, we implement a general method to compute the helicity flux density, G_Φ . Our aim is to validate the method and study the properties of G_Φ on case studies before applying it to observational studies. In order to interpret the G_Φ maps we will obtain in observational studies, we need to know the helicity distribution associated to typical flux transport velocity fields and how the properties of the magnetic connectivity change these helicity distributions. We also need to know how the different parameters used for the G_Φ computation can influence the results (*e.g.*, resolution of the magnetograms and G_θ maps, precision used for field lines integration).

To compute G_θ from Equation (4), we need the normal component of the magnetic field and the relative rotation rate of elementary magnetic flux tubes on \mathcal{S} . The extra information needed to compute G_Φ is the magnetic field in \mathcal{V} .

3.1. Flux Transport Velocity

Observations (*e.g.*, Moon *et al.*, 2002; Nindos, Zhang, and Zhang, 2003; Chae, Moon, and Park, 2004; Schuck, 2006; Jeong and Chae, 2007; LaBonte, Georgoulis, and Rust, 2007; Welsch *et al.*, 2009; Jing *et al.*, 2012) have reported complex patterns of photospheric flux transport velocities during the lifetimes of ARs involving the combination of separations and rotations of the entire or of parts of the magnetic polarities. In the following, we consider some elementary photospheric relative motions of two connected opposite magnetic polarities: two separating polarities without any rotation, a polarity rotating around another one, and two counter-rotating polarities. The polarities are isolated and magnetic-flux balanced. We consider a cartesian domain centered on point O (see Figure 1). The positive (P_+) and negative (P_-) polarities are centered on O_+ and O_- on the x -axis, respectively. The polarities are separated by the distance $D = |\mathbf{O}_+ \mathbf{O}_-|$.

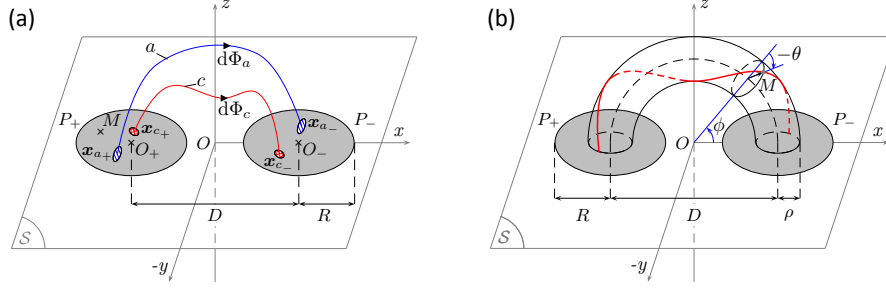


Figure 1. (a) Sketch of the general magnetic configuration considered in our models constructed with two opposite and magnetic-flux balanced polarities, P_+ and P_- . The S -surface ($z = 0$ -plane) symbolizes the photosphere. The two magnetic field lines “ a ” (blue line) and “ c ” (red line) show the general connectivity. The magnetic field lines “ a ” and “ c ” go from magnetic footpoints x_{a+} and x_{c+} on S to magnetic footpoints x_{a-} and x_{c-} with magnetic fluxes $d\Phi_a$ and $d\Phi_c$, respectively. (b) Scheme of the torus configuration. The two polarities (P_+ and P_-) are the bases of the torus. The red line represents a magnetic field line of the torus at a radius ρ from its axis.

The considered flux transport velocity field at point $M(\mathbf{x})$ for the two separating polarities model is:

$$\mathbf{u}(M) = \mp U_0 \mathbf{e}_x, \quad \text{for } \pm B_n(M) > 0, \quad (11)$$

where U_0 is a positive constant. The associated helicity flux density G_θ is therefore (see Appendix A.1 for a detailed derivation):

$$G_\theta(M) = \frac{U_0 B_n(M)}{\pi} \frac{\mathbf{O}_\mp \mathbf{M} \cdot \mathbf{e}_y}{|\mathbf{O}_\mp \mathbf{M}|^2} \Phi_0, \quad \text{for } \pm B_n(M) > 0, \quad (12)$$

where Φ_0 is the absolute value of the total magnetic flux of each polarity.

For the model of the negative polarity rigidly rotating around the positive one, the flux transport velocity field is:

$$\mathbf{u}(M) = \boldsymbol{\Omega} \times \mathbf{O}_+ \mathbf{M}, \quad \text{for } B_n(M) < 0, \quad (13)$$

where $\boldsymbol{\Omega} = \Omega \mathbf{e}_z$, Ω being the positive constant rotation rate of the negative polarity. From Appendix A.2, the associated helicity flux density is non-zero only if M is in the positive polarity, and its expression is given by:

$$G_\theta(M) = -\frac{\Omega B_n(M)}{2\pi} \frac{\mathbf{O}_- \mathbf{M} \cdot \mathbf{O}_+ \mathbf{O}_-}{|\mathbf{O}_- \mathbf{M}|^2} \Phi_0, \quad \text{for } B_n(M) > 0. \quad (14)$$

For the third motion model — *i.e.*, two counter-rotating opposite magnetic polarities — the flux transport velocity field is:

$$\mathbf{u}(M) = \mp \boldsymbol{\Omega} \times \mathbf{O}_\pm \mathbf{M}, \quad \text{for } \pm B_n(M) > 0, \quad (15)$$

resulting in a helicity flux density (see Appendix A.3):

$$G_\theta(M) = \mp \frac{\Omega B_n(M)}{2\pi} \frac{\mathbf{O}_\mp \mathbf{M} \cdot \mathbf{O}_+ \mathbf{O}_-}{|\mathbf{O}_\mp \mathbf{M}|^2} \Phi_0, \quad \text{for } \pm B_n(M) > 0. \quad (16)$$

3.2. Magnetic Field

Because we want to estimate the precision of the method, it is worthwhile to first consider simple analytical magnetic fields for which the connectivity is theoretically known. This allows us to estimate the precision of our computing method of G_Φ .

One simple analytical field to start with is a potential magnetic field (see Figure 2a). Such a field is constructed by placing two artificial opposite magnetic charges below the photosphere. The positive and negative magnetic charges are placed at A_+ and A_- , resulting in:

$$\mathbf{B}(\mathbf{x}) = q_0 \frac{\mathbf{x} - \mathbf{x}_+}{|\mathbf{x} - \mathbf{x}_+|^3} - q_0 \frac{\mathbf{x} - \mathbf{x}_-}{|\mathbf{x} - \mathbf{x}_-|^3}, \quad (17)$$

where $\mathbf{x}_\pm = \mathbf{O}\mathbf{A}_\pm$ and q_0 is the absolute value of the positive and negative magnetic charges.

Theoretical and numerical simulations studies have shown that, to emerge into the corona, a magnetic flux tube needs some twist (Emonet and Moreno-Insertis, 1998). Observational studies also highlight that as an AR appears, important amounts of helicity are injected into the corona (*e.g.*, Chae, 2001; Kusano *et al.*, 2004b; Pariat *et al.*, 2006; Jeong and Chae, 2007; Romano *et al.*, 2011; Jing *et al.*, 2012), with evidences of a twisted flux tube (Luoni *et al.*, 2011). Therefore, we consider a second magnetic field defined by a uniformly twisted torus half-emerged into the corona (see panels b and d of Figure 2; Luoni *et al.*, 2011). The associated magnetic field is $\mathbf{B} = B_\theta \mathbf{e}_\theta + B_\phi \mathbf{e}_\phi$, such that:

$$\begin{aligned} B_\theta(M) &= \frac{4N\rho}{D + 2\rho\cos(\theta)} B_\phi(M), \\ B_\phi(M) &= -B_0 e^{-(\rho/R)^2}, \end{aligned} \quad (18)$$

where N corresponds to the number of turns of the magnetic field lines around the torus axis in half the torus, and B_0 is the magnetic field strength at the center of the positive polarity. The torus center is located at photospheric point O , and the distance $D/2$ defines the main radius of the torus. The variables ρ , θ and ϕ are respectively the distance to the torus axis, the rotation angle around the torus axis, and the location angle along the torus axis (see Figure 1b).

For the two previous cases, the magnetic field is analytical. However, extrapolations of observed magnetograms are in most cases non-analytical fields given on a discrete mesh. The consequence is that errors due to extrapolations and interpolations of the magnetic field will possibly degrade or modify the signal in G_Φ maps. To investigate it, we performed linear force-free field extrapolations (see Figures 2c and 2e) of a magnetogram defined by:

$$\mathbf{B}_{z=0}(M) = \pm B_0 \mathbf{e}_z, \quad \text{for } M \text{ in } P_\pm, \quad (19)$$

where B_0 is the magnetic field strength in the positive polarity and, P_+ and P_- refer to the positive and negative magnetic polarities which are circular

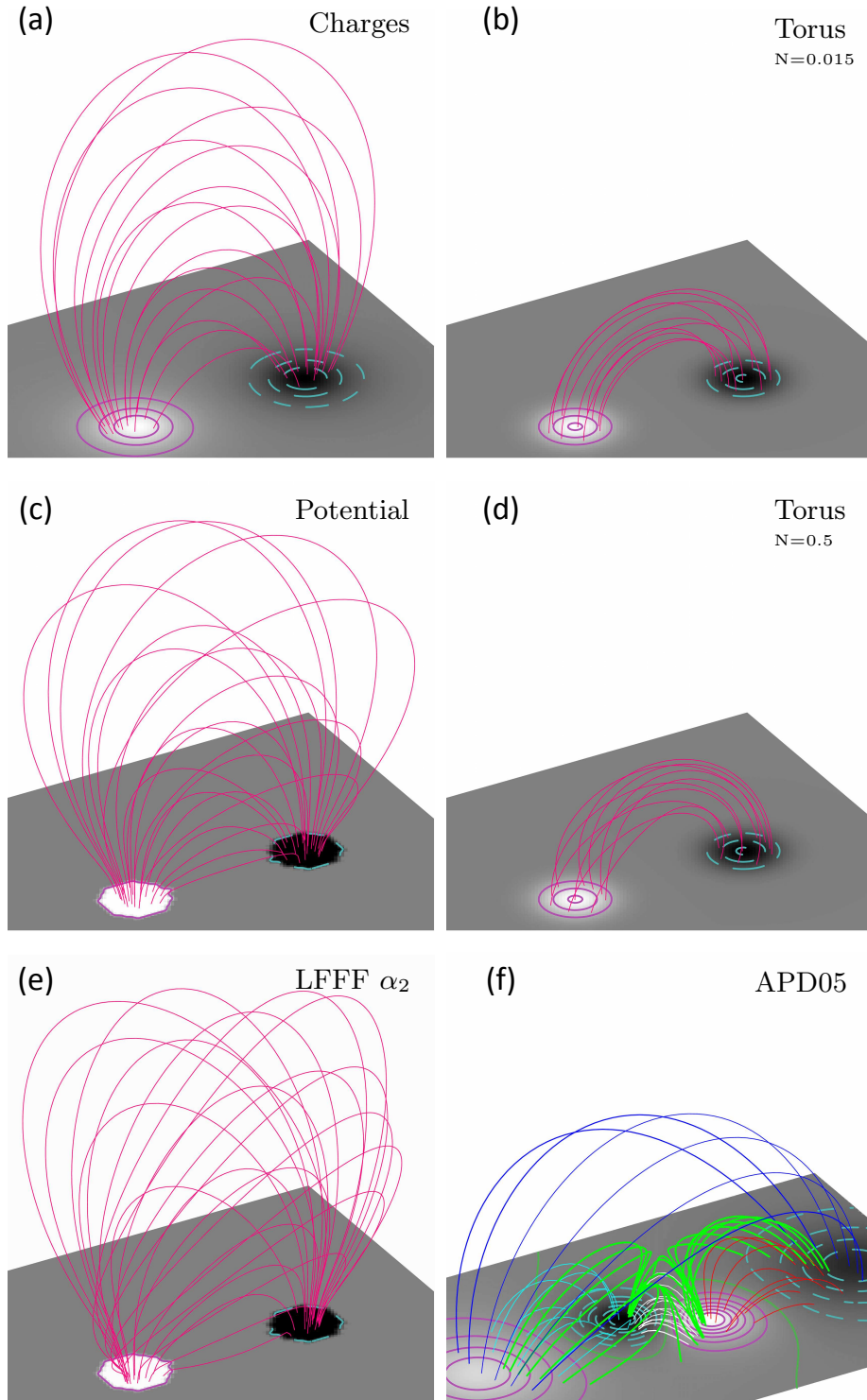


Figure 2. Magnetic field configurations considered in our investigations. The magnetograms are represented at the $z = 0$ plane with superposed isocontours of the magnetic field (cyan dashed and purple solid-lines for negative and positive values of the magnetic field respectively). For all but panel (f), the magnetic field lines are represented by the pink lines and the magnetic field values are between 1000 Gauss (white) and -1000 Gauss (black). (a) Two magnetic charges. (b,d) Half-emerged torus with a twist $N = 0.015$ and $N = 0.5$ respectively. (c,e) Two uniform opposite magnetic polarities with linear constant- α force-free field extrapolations $\alpha = 0$ and $\alpha = 5.6 \times 10^{-3} \text{ Mm}^{-1}$ respectively. (f) MHD simulation of a magnetic configuration with quasi-separatrix layers (QSLs). Different colors (red, white, cyan and blue) have been used to show the different quasi-domains of connectivity. Thick green magnetic field lines correspond to QSLs field lines (see Section 7). The S-like green line on the magnetogram corresponds to the polarity inversion line.

of radius R (cf Figure 1a). The extrapolations were performed using the code XTRAPOL (*e.g.*, Amari, Boulmezaoud, and Mikic, 1999; Amari, Boulmezaoud, and Aly, 2006; Amari and Aly, 2010). The code solves the Poisson’s equation for the vector potential, $\nabla^2 \mathbf{A} + \alpha^2 \mathbf{A} = 0$, with the boundary conditions given by Equation (19) inside the photospheric polarities and $\mathbf{B} \cdot d\mathcal{S} = 0$ elsewhere on the boundaries of the extrapolation domain. The vector potential formulation ensures that the solenoidal condition is verified to the machine precision. The boundary conditions assumes that no field go through the lateral and top boundaries. This imposes that the total magnetic flux within the positive polarity is entirely connected to the negative polarity. We make this choice to prevent the presence of open magnetic field lines in the domain in order to compute G_Φ for all photospheric magnetic footpoints of G_θ maps. Note also that, the spatial resolution of the extrapolated fields is chosen to be different from the one used to compute G_θ (see the fragmented shape of the magnetic field isocontours in Figures 2c and 2e). We make this choice to investigate the effect of using a different resolution between the extrapolations and the helicity flux density maps. In practice, we find no significant effects as long as the difference of resolution is lower than 8 for our high resolution helicity flux density maps. This means that we can use a lower resolution in the extrapolation without modifying the resulting G_Φ map.

The last magnetic configuration considered is more complex as it involves quasi-separatrix layers in MHD simulations. This magnetic field and the associated flux transport velocity fields will be described in Section 7.

For the extrapolated magnetic fields, the magnetic flux is restricted to two circular regions (as defined in Figure 1a). However, this is not strictly the case for the two analytical magnetic fields: even if the field strength strongly decreases away from O_\pm , it does not vanish. Consequently, there is helicity signal in the whole domain considered in the G_θ and G_Φ maps for the analytical magnetic fields of Equations (17) and (18) as illustrated for G_θ in Figure 3a. For coherence

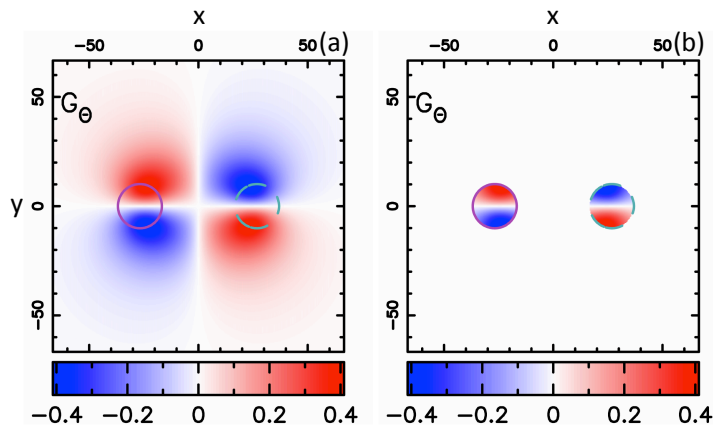


Figure 3. (a) Full G_θ map of the analytical potential magnetic field (Equation (17)). (b) G_θ map for the considered polarities with positive (solid purple) and negative (dashed cyan) isocontours of the magnetic field delimiting these two polarities.

of the results, we always extract and consider the helicity flux signal from the two connected polarities of radius R as shown in Figure 3b, and which contain most of the magnetic flux. From now on, the positive and negative polarities P_+ and P_- will refer to these two polarities, and all scalings of Section 3.3 are made with respect to them. However, it must be emphasized that, in all our models, G_Φ computation takes into account the motion of all the magnetic flux at $z = 0$.

3.3. Numerical Setup

All maps are computed in a cartesian domain with 400×400 points. The scaling is chosen to take into account the typical values obtained from observations. The $z = 0$ -plane, which represents the photosphere, covers the xy -domain $[-67, 67] \times [-67, 67]$ Mm². The centers of the photospheric polarities are separated by the distance $D = 54$ Mm. The positive and the negative magnetic charges are placed at points A_+ of coordinates $(-27, 0, -13)$ Mm and A_- of coordinates $(27, 0, -13)$ Mm, respectively. The radius of the photospheric polarities is set to $R = 10$ Mm. The maximum value of the normal component of the magnetic field, B_0 , and of the flux transport velocity fields, U_0 , are set to 1000 Gauss and 0.1 km s^{-1} respectively. The extrapolations were performed on a non-uniform mesh covering the domain $[-533, 533] \times [-533, 533] \times [0, 1066]$ Mm³ with $513 \times 513 \times 200$ points.

The above scalings lead to helicity flux densities in units of $10^6 \text{ Wb}^2 \cdot \text{m}^{-2} \cdot \text{s}^{-1}$, and a total helicity flux in units of $10^{21} \text{ Wb}^2 \cdot \text{s}^{-1}$ which are typical observed values in ARs (*e.g.*, Chae, 2001; Chandra *et al.*, 2010).

G_θ maps are computed using Equations (11) – (19). Let us first consider the positive magnetic polarity ($B_n > 0$). In practice, each G_θ -mesh point \mathbf{x}_{a+} , is identified as the cross-section of an elementary magnetic flux-tube with the photosphere and is associated to the surface helicity flux density $G_\theta(\mathbf{x}_{a+})$ at this point. To compute $G_\Phi(\mathbf{x}_{a+})$, we need the position of \mathbf{x}_{a-} — the second footpoint of the elementary magnetic flux-tube “ a ” — and its associated surface helicity flux density. Each elementary magnetic flux-tube is thus associated to one magnetic field line that is integrated to get the connectivity. The integration is performed starting from \mathbf{x}_{a+} to \mathbf{x}_{a-} using the Fortran NAG-routine D02CJF, with the precision of the integration defined as 10^{-n} . Thus, the higher n is, the more precisely the connectivity and G_Φ are computed. Generally, the \mathbf{x}_{a-} footpoint does not fall on a mesh point. Thus, the values of G_θ and B_n at this point are bilinearly interpolated using the values at the four closest surrounding mesh points. If \mathbf{x}_{a-} is not found on the ($z = 0$)-plane (*e.g.*, open magnetic field lines), the value of G_Φ at \mathbf{x}_{a+} is simply set to $G_\theta(\mathbf{x}_{a+})$. Finally, the same procedure as above is used in the negative magnetic polarity ($B_n < 0$) starting the magnetic field line integration from \mathbf{x}_{a-} .

4. Results for Two Magnetic Charges

In this section, the magnetic field is given by Equation (17) for all flux transport velocity models and the associated magnetogram at the $z = 0$ -plane is displayed in Figure 2a.

4.1. Two Separating Magnetic Polarities

In this example, the two connected opposite magnetic polarities separate away from each other in the x -direction (see Equation (11)). Since the polarities simply separate without any rotation, no helicity is injected to the system. However, as the two polarities separate, every elementary polarity sees a relative rotation of all other elementary polarities of opposite sign. This induces net non-zero values of G_θ as shown in the left panel of Figure 4a.

In this model, the symmetry of the magnetic field and of the applied velocity field implies $G_\theta(\mathbf{x}_{a-}) = -G_\theta(\mathbf{x}_{a+})$. Therefore, by taking the connectivity into account, G_Φ is null to the numerical errors over all the two polarities (Figure 4b). This simple example reveals the limits of G_θ to present a truthful distribution of helicity flux while G_Φ gives the expected results.

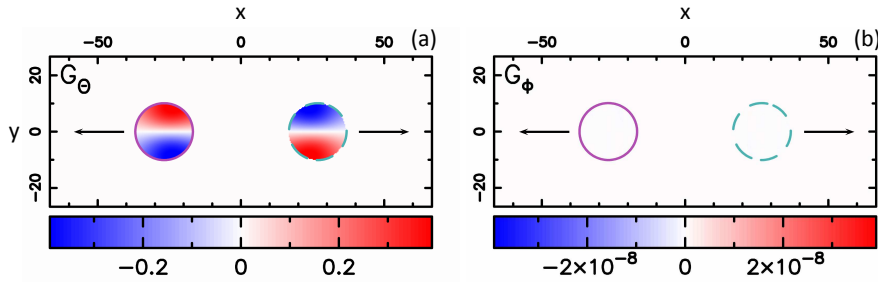


Figure 4. Helicity flux density distribution, in $10^6 \text{ Wb}^2\text{m}^{-2}\text{s}^{-1}$, for the case of two separating opposite magnetic polarities without rotation. (a) G_θ map. (b) G_Φ map. Solid purple and dashed cyan are isocontours of the magnetic field. Black arrows show the motion applied to the polarities. The saturation levels of G_θ and G_Φ are different by eight orders of magnitude.

4.2. One Polarity Rigidly Rotating Around the Other

The positive polarity is fixed while the negative polarity rigidly rotates around O_+ (the center of the positive polarity, see Equation (13)). From Equation (14),

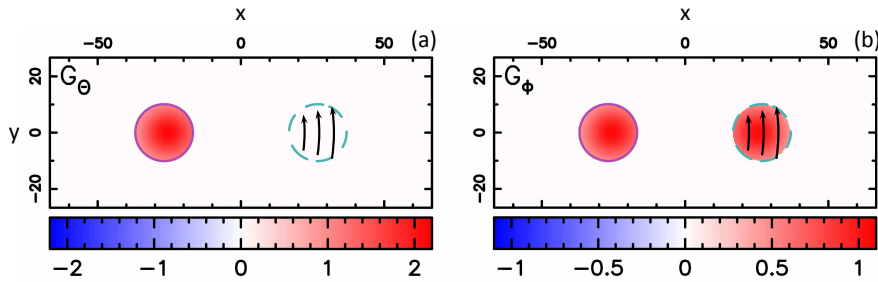


Figure 5. Helicity flux density distribution, in $10^6 \text{ Wb}^2\text{m}^{-2}\text{s}^{-1}$ for the negative polarity rigidly rotating around the positive polarity. The drawing convention is the same as in Figure 4 (with a different color scale).

G_θ is non-zero only in the positive polarity. The reason is that, in Equation (4), there are two terms that contribute to G_θ inside one polarity. One term is the relative motion of footpoints inside the polarity. The second is the relative motion with regard to the footpoints of the other polarity. In the negative polarity, the two terms cancel out (Appendix A.2). In the positive polarity, however, only the term coming from the relative motion of the negative polarity is non-zero.

This second example also presents the limits of G_θ maps to well localize the injection of helicity. This can be misleading when relating the injection of helicity to magnetic activity (*e.g.*, Chandra *et al.*, 2010). This is corrected in the corresponding G_Φ map that shows that positive helicity is redistributed in both polarities (Figure 5b).

4.3. Two Counter-rotating Polarities

Let us now consider the model of two counter-rotating polarities (Equation (15)). The positive and negative polarities rigidly rotate clockwise and counterclockwise around their centers O_+ and O_- , respectively. This configuration illustrates the difference of assumptions in the definition of G_θ and G_Φ .

Indeed, if the rotation is slow enough, the system is equivalent to a non-twisted flux tube rotating around its central axis. With such driving, a non-twisted flux tube would appear similarly untwisted at any time. Thus, overall no helicity is injected to the system. One therefore expects that G_Φ would correspond to this null injection of magnetic helicity.

The G_θ map presents a distribution of helicity which is far different from a null injection (Figure 6a). Taking the connectivity into account, *i.e.*, using G_Φ (Figure 6b), removes this helicity flux signal (regardless of numerical errors) allowing to get the expected null distribution of helicity flux.

While G_θ clearly misrepresents the global slow injection of helicity in this case, it would properly represent the helicity injection if the considered motion was extremely fast. Indeed if one considers counter rotating motions at a speed higher than the Alfvénic transit time, the opposite footpoint would have no indication of the helicity injection at the other footpoint. At the beginning of the injection, an initially untwisted flux rope would be such that the central part

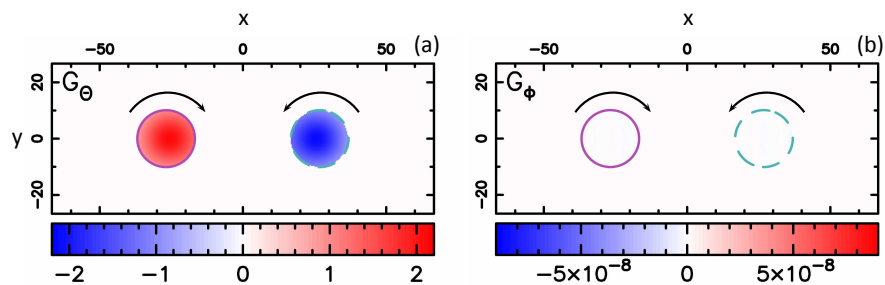


Figure 6. Helicity flux density distribution, in $10^6 \text{ Wb}^2\text{m}^{-2}\text{s}^{-1}$ for the two counter-rotating opposite magnetic polarities. The drawing convention is the same as in Figure 4 (with a different color scale).

would stay untwisted but with oppositely twisted field around each footpoint. These counter-rotating motions would correspond to the launch of two rotating Alfvén waves of opposite sign. The G_θ maps do properly represent such helicity injection. As time goes, these Alfvén waves would eventually cancel each other resulting in a null helicity budget for the system. For longer timescales, the G_Φ map therefore better represents the proper helicity injection in the system.

4.4. Errors Estimation

In this section, we investigate the role of the parameter n — used for field lines integration — in the above G_Φ maps. G_θ and the connectivity are analytically known which allows us to compute the theoretical value, $G_{\Phi,\text{th}}$. Then, we estimate the error between the computed G_Φ map from our numerical method and $G_{\Phi,\text{th}}$ by computing the root mean square of $G_\Phi - G_{\Phi,\text{th}}$.

With the analytical magnetic field considered in this section, the resolution on the magnetic field is only limited by the computing precision, *i.e.*, 10^{-16} as the magnetic field was computed with a double precision. The numerical precision on G_Φ is thus limited by the precision of:

- G_θ , $\text{err}_{G_\theta} \approx 10^{-16}$,
- the field lines integration, $\text{err}_{\text{fli}} \approx 10^{-n}$,
- the computation of B_n at the second footpoint, $\text{err}_{B_n} \approx 10^{-16}$,
- the bilinear interpolation of G_θ at the second footpoint, $\text{err}_{\text{interp}}$.

The total error at each mesh point, err_{tot} , can thus be estimated as follows:

$$\text{err}_{\text{tot}} \approx \sqrt{\text{err}_{G_\theta}^2 + \text{err}_{\text{fli}}^2 + \text{err}_{B_n}^2 + \text{err}_{\text{interp}}^2}. \quad (20)$$

For smooth variations of G_θ (as in all our cases), the error from the bilinear interpolation should not be the most limiting one. In this case, for $n < 16$, the precision on G_Φ is expected to be limited by the precision of field line integration. The consequence is that we expect an exponential decrease of the error as n increases.

Figure 7 displays the influence of n on the root mean square and the maximum error of G_Φ maps. As expected, the figure shows that both G_Φ rms and maximum error exponentially decrease as n increases. Therefore, the precision on G_Φ is indeed limited by the precision of field lines integration. The rms on G_Φ , for the three cases shown Figures 4 – 6 ($n = 8$), is 2, 5 and 7×10^{-10} G_θ units respectively, *i.e.*, more than 10^9 times smaller than the typical values of the signal found in G_θ maps. Hence, our numerical method allows us to compute the distribution of helicity flux, G_Φ , with a very good accuracy.

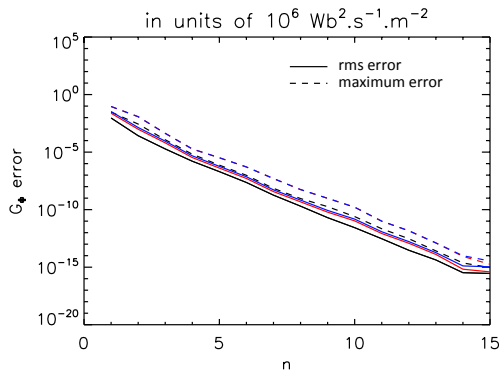


Figure 7. Computed root mean square (solid lines) and maximum error (dashed lines) from G_Φ maps for two separating polarities (black), the negative polarity rigidly rotating around the positive one (red), and two counter-rotating magnetic polarities (blue), as a function of the field line integration parameter n defining the numerical integration precision ($= 10^{-n}$).

5. Results for a Half Emerged Torus

In this section, the magnetic field is a uniformly twisted torus half emerged into the solar corona (see Figures 2b and 2d and Equation (18); Luoni *et al.*, 2011). The two opposite magnetic polarities are thus the two intersections of the torus with the photosphere (Figure 1b).

The amount of helicity, H , found in ARs can be converted to a uniform twist, N' , with $H = N'\Phi^2$, where Φ is the AR magnetic flux (average of both polarities). Observations report typical values of N' from ≈ 0.01 to ≈ 0.3 (Démoulin and Pariat, 2009 and references therein). In the following, we thus consider the torus configuration with $N = 0.015$, 0.05 , and 0.5 .

Note that, the case $N = 0$ has the same type of connectivity as the two magnetic charges but with a different B_n distribution. Therefore, we expect similar helicity flux distributions as in Figures 4 – 6 when the same velocity models are applied.

5.1. Two Separating Magnetic Polarities

As for the potential magnetic field of Section 4.1, the two polarities separate without any rotation (flow given by Equation (11)) implying that no helicity is injected to the system. As expected, G_θ (Figure 8a) exhibits a similar distribution as for the case with two magnetic charges (Figure 4a), and the total helicity flux computed from G_θ and G_Φ maps is indeed zero (Section 4.1). However, as shown by Figure 8b-d, G_Φ maps also present helicity injection with both signs of helicity in both polarities. But are these signals in G_Φ maps real, or are they spurious signals as in the G_θ map?

Démoulin, Pariat, and Berger (2006), show that the total magnetic helicity flux in \mathcal{V} can be written as the summation of the mutual helicity of all pairs of elementary magnetic flux tubes contained in \mathcal{V} , *i.e.*, the total magnetic helicity

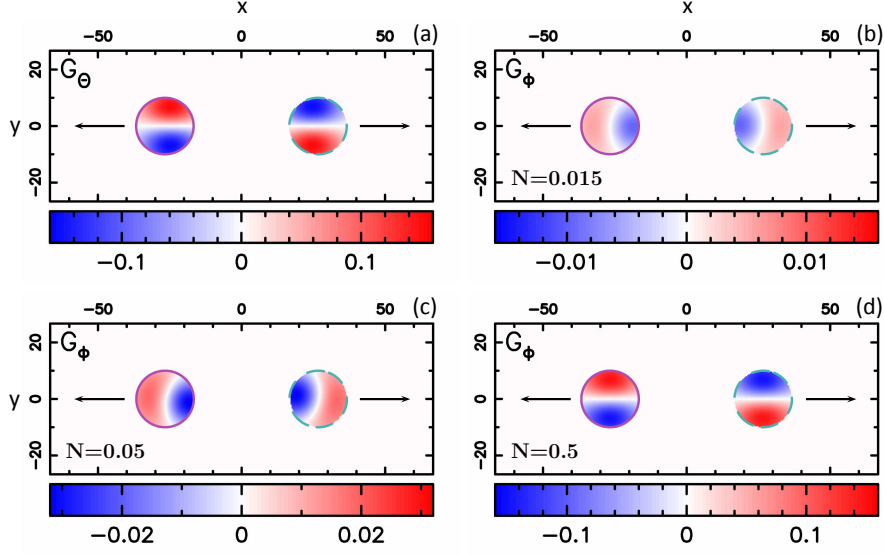


Figure 8. G_θ and G_Φ maps for the torus magnetic field configuration with two separating magnetic polarities. (a) G_θ map. (b,c,d) G_Φ maps for a twist $N = 0.015, 0.05$ and 0.5 respectively. The drawing convention is the same as in Figure 4 (notice the different color scales).

of the system can be rewritten as:

$$H = \frac{1}{2\pi} \int_{\Phi_\pm} \int_{\Phi_\pm} \mathcal{L}_{a,c} d\Phi_{a_+} d\Phi_{c_+}, \quad (21)$$

with $\mathcal{L}_{a,c}$, the mutual helicity between the two magnetic flux tubes “a” and “c”. Comparing the time derivative of Equation (21):

$$\frac{dH}{dt} = \frac{1}{2\pi} \int_{\Phi_\pm} \int_{\Phi_\pm} \frac{d\mathcal{L}_{a,c}}{dt} d\Phi_{a_+} d\Phi_{c_+}, \quad (22)$$

to Equations (7) and (8) implies:

$$\begin{aligned} \frac{d\mathcal{L}_{a,c}}{dt} &= \frac{d\theta(\mathbf{x}_{c_+} - \mathbf{x}_{a_-})}{dt} + \frac{d\theta(\mathbf{x}_{c_-} - \mathbf{x}_{a_+})}{dt} \\ &\quad - \frac{d\theta(\mathbf{x}_{c_+} - \mathbf{x}_{a_+})}{dt} - \frac{d\theta(\mathbf{x}_{c_-} - \mathbf{x}_{a_-})}{dt}. \end{aligned} \quad (23)$$

By integrating Equation (23) in time, they express the mutual helicity of two magnetic field lines “a” and “c” as a function of the angles between their photospheric footpoints. Using the convention that field line “c” is above field line “a”, they obtain:

$$\mathcal{L}_{a,c} = \mathcal{L}_{a,\tilde{c}}^{\text{arch}} = \frac{1}{2\pi} (\alpha_{c_+} + \alpha_{c_-}), \quad (24)$$

where $\alpha_{c_{\pm}}$ is the angle between segments $c_{\pm}a_{\pm}$ and $c_{\pm}a_{\mp}$ and is defined in the interval $[-\pi, \pi]$ with the trigonometric convention (Figure 9a). The consequence is that any change in these angles will lead to a variation of mutual helicity and thus, a flux of magnetic helicity (Equations (22) – (24)).

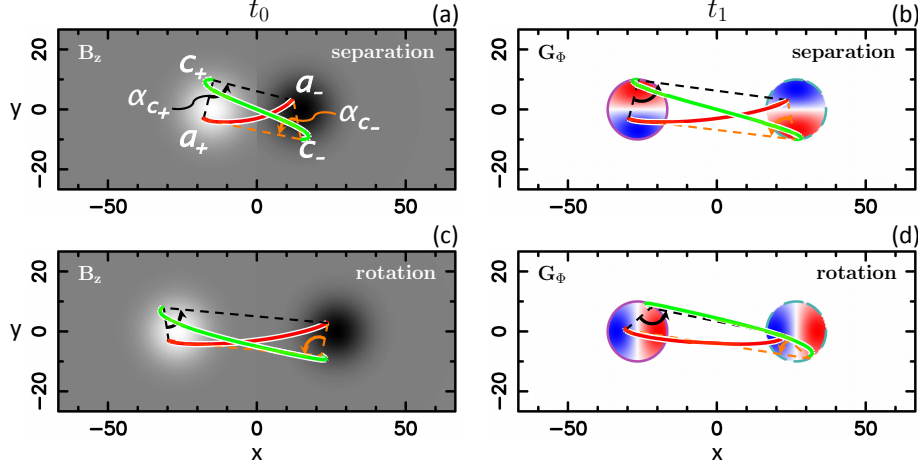


Figure 9. Torus configuration for the twist $N = 0.5$ illustrating the change in mutual magnetic helicity between two magnetic field lines (red and green lines) at two different times ($t_1 > t_0$) and at $z = 0$. (a,b) Two separating magnetic polarities (as in Figure 8). (c,d) Counter-rotating polarities (as in Figure 10). *Left column:* Normal component of the magnetic field at t_0 . The values of the magnetic field are in the range -1000 G (black) to 1000 G (white). *Right column:* Distribution of G_{Φ} at t_1 . The angle between segments $c_{\pm}a_{\pm}$ and $c_{\pm}a_{\mp}$ represents the angle $\alpha_{c_{\pm}}$ of Equation (24). The change in the relative orientation of the red and green magnetic field lines that leads to the change in $\alpha_{c_{\pm}}$ — right panel compared with left panel — is a clear evidence of mutual magnetic helicity changes of the two field lines between t_0 and t_1 .

Let us consider the two magnetic field lines “a” and “c” starting at a_+ and c_+ and ending at a_- and c_- , respectively represented by the red and green lines in Figure 9 of the torus for $N = 0.5$. As the two polarities of the torus separate away from each other in the x -direction, the y -coordinate of all four footpoints remains unchanged. Hence, the orientation of the segments $c_{\pm}a_{\pm}$ remains also the same, and only segments $c_{\pm}a_{\mp}$ change of orientation. In particular, the geometry implies that $\alpha_{c_{\pm}}$ increases as the polarities separate in the case shown in Figure 9 for $N = 0.5$. Therefore, the separation induces a positive variation of mutual helicity of “a” and “c”.

More generally, there is always an increase of mutual helicity of the magnetic field line “c” in Figures 9a and 9b with any other magnetic field line “a” inside the polarities: as the polarities separate, there is always an increase of $\alpha_{c_{\pm}}$ for any “a” within the polarities. This results in a net positive change of mutual helicity for “c” with regard to all the other “a”, and thus, a net positive helicity flux G_{Φ} at the footpoint location of “c”.

A more precise geometrical analysis — *i.e.*, using the general definition of $\mathcal{L}_{a,c}$ in Equation (32) of Démoulin, Pariat, and Berger (2006) — reveals that, for the magnetic field lines footpoints of the $y > 0$ (resp. $y < 0$) part of the positive

polarity, there is a net positive (resp. negative) variation of mutual helicity with a magnitude decreasing with y (resp. increasing with $-y$).

For N close to 0 [1] (*i.e.*, modulo 1) turn, there is a similar behavior, except that the origin $O = (0, 0)$ is no longer a center of symmetry for the magnetic footpoints. In particular, at these values of N , we find that, for the most externe (resp. interne) magnetic field lines, there is a net positive (resp. negative) variation of mutual helicity leading to a net positive (resp. negative) helicity flux (Figure 8). However, the helicity flux at these N values is typically ten times smaller when $N = 0.015$ [1] than for the $N = 0.5$ [1] case. As N gets closer to 0.5 [1] turn, the magnetic field lines are more twisted and they share more mutual helicity, *i.e.*, the angles between the footpoints of two field lines are larger. The consequence is that, the change in the angles between footpoints, *i.e.*, in their mutual helicity, will be higher as the two polarities separate, tending towards the helicity flux distribution of Figure 8 as N gets closer to 0.5 [1] turn.

Therefore, the signal in the G_{Φ} maps of Figure 8 is due to a variation of mutual helicity between magnetic field lines as the two polarities separate, and thus, is a real signal.

5.2. One Polarity Rigidly Rotating Around the Other

The flux transport velocity field is given by Equation (13). As in Section 4.2, the helicity flux density distribution computed using G_{θ} only presents helicity flux in the positive polarity as in Figure 5a. The computation of helicity injection using G_{Φ} removes this problem and the associated flux is typically twice smaller than in G_{θ} , but present on both polarities independently of N value (comparable to Figure 5b).

5.3. Two Counter-rotating Polarities

As pointed out in Section 4.3, for slow enough motions of the flux transport velocity field (given by Equation (15)), this model is equivalent to a cylinder rotating around its axis. The only difference is that, now, the cylinder has twisted magnetic field lines. The presence of twisted field lines, though, does not change the fact that no helicity is globally injected to the system.

The instantaneous footpoint injections displayed by the G_{θ} map, Figure 10a, are similar to those in Figure 6a. They would be meaningful for very fast motions.

Considering G_{Φ} maps, the distribution changes significantly depending on the degree of twist (Figure 10). While the global injection stays null, G_{Φ} maps reveal subtle effects of mutual helicity variation between the twisted lines within the flux rope. Because of the twist, the magnetic field lines of the torus share mutual helicity between each other as the flux rope globally rotates around its axis. In a way similar to what has been discussed in Section 5.1, as the two polarities counter-rotate, the relative orientation of the magnetic field lines within the flux rope changes: *cf.* Figures 9c and 9d. The magnitude of this variation increases with the number of turns, N , of the magnetic field lines around the torus axis. This induces a net change of mutual helicity between the magnetic field lines revealed by the G_{Φ} maps of Figure 10. This process is completely hidden by the G_{θ} maps which are completely independent of the twist amount.

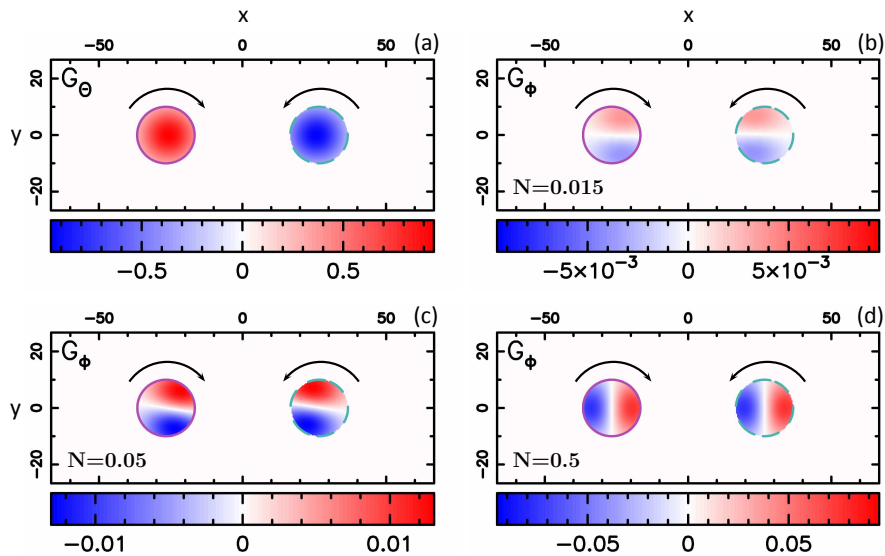


Figure 10. G_θ and G_Φ maps for the torus magnetic field configuration with two counter-rotating magnetic polarities. (a) G_θ map. (b,c,d) G_Φ maps for $N = 0.015$, 0.05 and 0.5 respectively. The drawing convention is the same as in Figure 4 (notice the different color scales).

The use of G_Φ is here crucial to understand the variation of mutual magnetic helicity driven by photospheric footpoint motions.

6. Results for Extrapolated Magnetic Fields

In observational studies, extrapolations of the magnetic field will be used to infer the connectivity. Hence, in our tests, we consider extrapolated magnetic fields in order to study the influence of using them on the precision of the connectivity and thus, of G_Φ .

In this section, we consider two uniform opposite magnetic polarities with $B_0 = 1000\text{ G}$ in the positive polarity and -1000 G in the negative polarity. Three linear force-free fields are considered in all our three flux transport velocity fields investigated: a potential field, and two linear force-free fields with a force-free parameter equal to $\alpha_1 = 10^{-3}$ and $\alpha_2 = 5.6 \times 10^{-3}\text{ Mm}^{-1}$ (Figures 2c and 2e) which are typical values derived from observations (see *e.g.*, Pevtsov, Canfield, and Metcalf, 1995; Longcope and Pevtsov, 2003; Green *et al.*, 2002b; Chandra *et al.*, 2010).

6.1. Two Separating Magnetic Polarities

In this section, we study the distribution of helicity flux density for the two separating magnetic polarities case (see Equation (11)).

First, let us consider the potential field ($\alpha = 0$, Figure 11b). With this magnetic field configuration, the model is analogous to the one considered Section 4. Consequently, as in Section 4.1, we expect no signal in the G_Φ map as no helicity is injected to the system. This is well shown in Figure 11b where the helicity flux signal is indeed null to the numerical errors.

Let us now consider the two linear force-free magnetic field configurations. These configurations are analogous to the torus one (for $N \neq 0$) in the sense that magnetic field lines now have non-null mutual helicity. Therefore, as the two polarities separate away from each other, the angles between magnetic field lines footpoints change. This results in a variation of mutual helicity between field lines inducing a local flux of magnetic helicity as shown in Figures 11c and 11d. However, the total helicity flux is indeed zero as expected (Section 5.1).

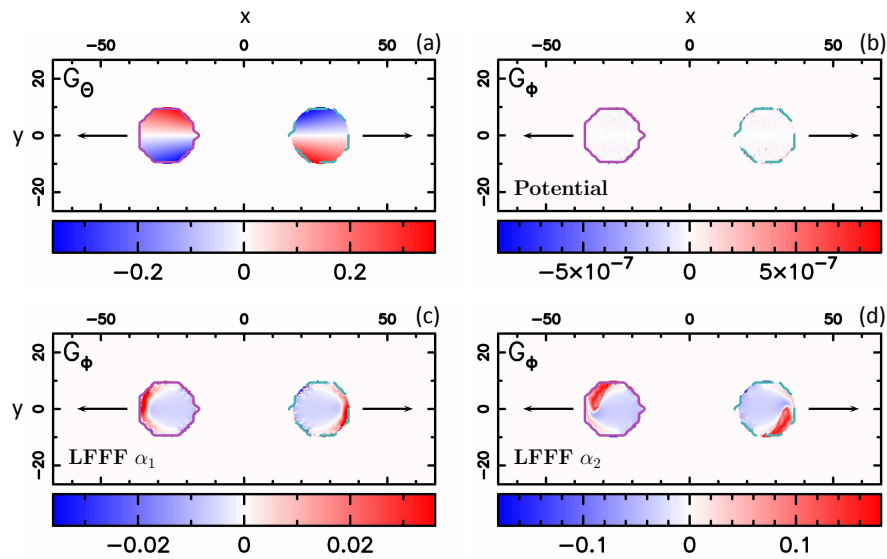


Figure 11. G_θ and G_Φ maps for the extrapolated magnetic field configurations with two separating magnetic polarities. (a) G_θ map. (b,c,d) G_Φ maps for the linear force-free fields $\alpha = 0$ (potential), $\alpha_1 = 10^{-3}$ and $\alpha_2 = 5.6 \times 10^{-3} \text{ Mm}^{-1}$. The drawing convention is the same as in Figure 4 (notice the different color scales).

Note also that, while the G_θ map exhibits, in each polarity, two regions of strong net opposite helicity flux (symmetric with regard to the x -axis), the G_Φ maps present a diffuse (concentrated) region of negative (positive) flux in the inner (most external) part of the system, respectively. In addition, the higher the linear force-free field constant α is (in magnitude), the higher is the magnitude of the helicity flux signal in each polarity. These results are in agreement with the ones for the torus case and, again, demonstrate the limits of the G_θ proxy.

6.2. One Polarity Rigidly Rotating Around the Other

In this section, the negative polarity rigidly rotates around the center of the positive polarity (Equation (13)).

Because G_θ does not take the magnetic field lines connectivity into account, it is not able to show that helicity is injected in both magnetic polarities. As in Sections 4.2 and 5.2, G_Φ proxy displays the true distribution of helicity flux, which is positive in both positive and negative polarities and twice smaller than with G_θ in the positive polarity (comparable to Figure 5).

6.3. Two Counter-rotating Polarities

The two opposite magnetic polarities are counter-rotating around their own center (Equation (15)). We recall that this model is equivalent to the rotation of a cylinder around its axis, and hence, no helicity is globally injected to the system.

For the same reasons as in Section 4.3, the G_Φ map of the potential magnetic field case has zero values (to the numerical errors) everywhere. As indicated by Figure 12, the G_Φ maps for the two linear force-free fields ($\alpha \neq 0$) present non-zero helicity fluxes with both signs in both polarities. As for the torus case ($N \neq 0$), the signal in G_Φ maps is real as there is a change of mutual helicity between magnetic field lines as the two polarities rotate.

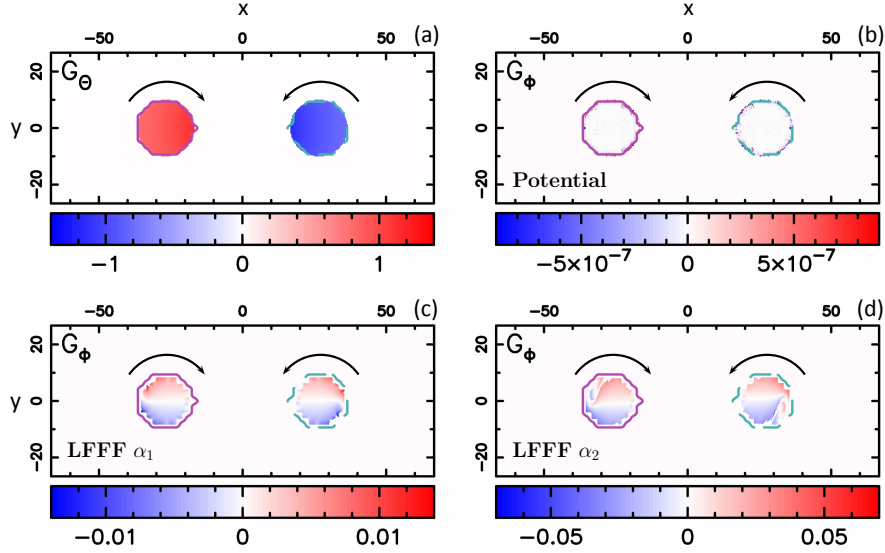


Figure 12. G_θ and G_Φ maps for the extrapolated magnetic field configurations with two counter-rotating magnetic polarities. (a) G_θ map. (b,c,d) G_Φ maps for the linear force-free fields $\alpha = 0$ (potential), $\alpha_1 = 10^{-3}$ and $\alpha_2 = 5.6 \times 10^{-3} \text{ Mm}^{-1}$. The drawing convention is the same as in Figure 4 (notice the different color scales).

6.4. Errors Estimation

As in Section 4.4, we estimate the computation errors due to the magnetic field lines integration as a function of the field lines integration parameter n . An analytical connectivity is available for the potential field since it has the same

type of connectivity as the two magnetic charges (although with a different B_n distribution). Then, it is straightforward to compute the theoretical $G_{\Phi, \text{th}}$ value for each flux transport velocity model and the errors.

As expected, Figure 13 shows that both G_{Φ} rms and maximum error exponentially decrease as n increases. However, it also shows a saturation of the errors to $10^{-6} - 10^{-4} G_{\theta}$ units for $n > 6$. In particular, the rms on G_{Φ} (black, red and blue solid lines) saturate at $0.2, 7$ and $8 \times 10^{-5} G_{\theta}$ units respectively.

The use of an extrapolated magnetic field implies that the magnetic field is discretized. Hence, at each step of the integration of magnetic field lines, the magnetic field is interpolated and not analytically computed. This affects the precision on the computation of B_n and G_{θ} at the second footpoint of each magnetic field line, *i.e.*, enhances the terms err_{B_n} and $\text{err}_{\text{interp}}$ in Equation (20). This is well illustrated in Figure 13 where the choice of n dominates the precision of G_{Φ} only up to $n = 6$. Even though the precision reached on G_{Φ} is much less for $n > 6$ than in the potential analytical case (Section 4), our method still allows us to compute the true distribution of helicity injection with a good accuracy.

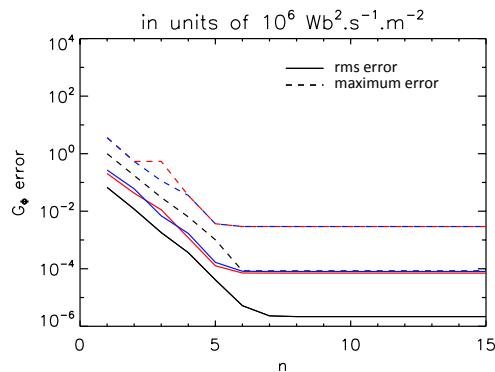


Figure 13. Computed root mean square (solid lines) and maximum error (dashed lines) from G_{Φ} maps as a function of the field line integration parameter n defining the numerical integration precision ($= 10^{-n}$). This plot is similar to Figure 7 but done for an extrapolated potential field. Three boundary flows are shown: two separating polarities (black), the negative polarity rigidly rotating around the positive one (red), and two counter-rotating magnetic polarities (blue).

7. Results for Magnetic Fields Containing Quasi-separatrix Layers

In this section, we investigate the helicity injection at the $z = 0$ -plane in two quadrupolar magnetic field configurations with quasi-separatrix layers (QSLs), from the simulations of Aulanier, Pariat, and Démoulin (2005). Our goal is to study the quality of our method when strong connectivity gradients are present.

7.1. QSLs

QSLs are regions where the magnetic field lines connectivity changes continuously with very sharp gradients with the limit case of separatrices when gradients

are infinite (Démoulin, Priest, and Lonie, 1996; Titov, Hornig, and Démoulin, 2002). Even in the cases with continuous connectivity changes, QSLs are preferential sites for current layers formation (see Aulanier, Pariat, and Démoulin (2005) and references therein).

The concept of QSLs has been intensively studied and developed in the last two decades (see review by Démoulin (2006) and references therein) and observational data analyses have reported the presence of such topological structures in the solar atmosphere (*e.g.*, Démoulin *et al.*, 1997; Mandrini *et al.*, 1997, 2006; Bagalá *et al.*, 2000; Masson *et al.*, 2009; Baker *et al.*, 2009; Savcheva *et al.*, 2012). QSLs are defined as regions where the squashing degree, Q , is much larger than 2 (Titov, Hornig, and Démoulin, 2002). If we consider an elementary flux tube — within a QSL — with one circular photospheric footpoint, then Q is a measure of the squashing of the section of this elementary flux tube at the other photospheric footpoint. Configurations with QSLs are thus cases for which a connectivity-based helicity flux density is required to localize the true site(s) of helicity injection and, *e.g.*, study its role in the trigger of eruptive events.

7.2. Initial Magnetic Field Configurations and Flux Transport Velocities

In the following, we consider the magnetic field configurations from the simulations of Aulanier, Pariat, and Démoulin (2005) on the formation of current layers in QSLs (Figure 2f). The magnetic configurations are referred to as $\Phi = 120^\circ$ and $\Phi = 150^\circ$ where Φ describes the angle between the inner and outer dipoles. For each magnetic configuration, two flux transport velocity fields are considered: a nearly solid translation in the y -direction and a nearly solid rotation of the positive polarity of the inner dipole (see Sections 2,3 and Figure 5 of Aulanier, Pariat, and Démoulin (2005) for further detailed informations on the setup). For simplicity, the positive and negative polarities of the inner or outer dipole will be referred to as IP and IN, or OP and ON, respectively.

7.3. Results with Twisting Motions

In this model, the IP polarity nearly rigidly rotates counterclockwise around its center. The flux transport velocity field is given by Equations (13) and (14) of Aulanier, Pariat, and Démoulin (2005). In terms of helicity flux density, we can analytically show that $G_\theta(\mathbf{x}) = 0$ when \mathbf{x} is not in IP and $G_\theta(\mathbf{x} \text{ in IP}) < 0$. For G_Φ on the other hand, because the twisting motion is applied to one part of the QSLs, we expect to see two regions of a twice smaller helicity flux: in IP and in the part of the QSLs connected to it.

Figure 14 displays the results of the G_θ (top row) and G_Φ (middle row) computations for the $\Phi = 120^\circ$ (left column) and 150° (right column) configurations. As expected, G_θ maps present a negative helicity flux distributed only in IP.

In the G_Φ maps, two main distinct regions of negative helicity flux are present (Figures 14c and 14d). The first region, IP, has a flux twice smaller than in G_θ as expected (notice the factor 1/2 between G_θ and G_Φ color scales). The second region corresponds to the QSL portion connected to IP. The helicity flux is more concentrated on the edges of the QSL in both ON and IN (see G_Φ compared to

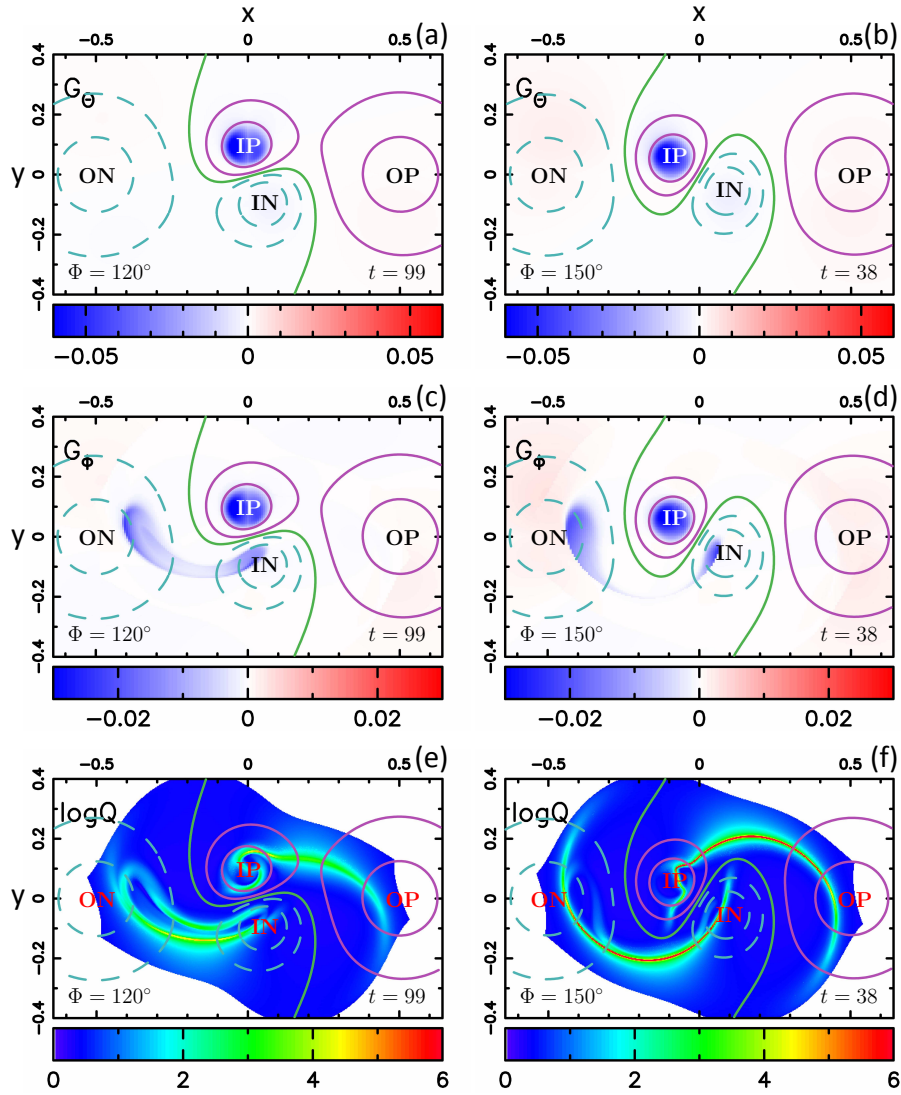


Figure 14. Results of two MHD simulations with a nearly solid rotation of the inner magnetic polarity (IP) and no motion in other polarities. The angle between the inner and outer bipoles is $\Phi = 120^\circ$ (left column) and $\Phi = 150^\circ$ (right column) and the simulation time is $t = 99$ and $t = 38$ Alfvén times respectively. The panels show the photospheric distribution of: (a,b) G_θ , (c,d) G_ϕ , and (e,f) $\log_{10}Q$. The green line corresponds to the polarity inversion line, while the solid purple (resp. dashed cyan) are positive (resp. negative) isocontours of the magnetic field.

$\log_{10}Q$ maps). This effect is even more important for the $\Phi = 150^\circ$ configuration (Figure 14d). This is due to the $|B_n(\mathbf{x}_{a_-})/B_n(\mathbf{x}_{a_+})|$ ratio which is much smaller than unity in between ON and IN. Hence, from Equation (10), it results that the helicity flux density is much weaker in the center of the QSL than at its edges. Because in the $\Phi = 120^\circ$ configuration, IN and ON are closer to each other, the region of weak B_n is smaller and the helicity flux distribution appears

less concentrated at the edges of the QSL than for the $\Phi = 150^\circ$ configuration (Figures 14c and 14d).

Finally, we notice that, the positive helicity flux signal in G_Φ maps (Figures 14c and 14d) is a remnant spurious signal already present in G_θ maps, as the velocity field is not numerically limited to IP.

7.4. Results with Translational Motions

Let us now consider the nearly translational motion of IP in the y -direction — given by Equation (12) of Aulanier, Pariat, and Démoulin (2005) — which leads to a global shearing of the configuration (Figure 15). We note that a small part of IN is also affected by the numerical setup (see the deformation of the isocontours of IN compared with the twisting case).

First, let us consider the $\Phi = 120^\circ$ case. The G_θ map (Figure 15a) shows a rather diffuse positive helicity injection in the outer dipole, a slightly more concentrated positive flux in IP, and a quasi-null flux around the IN except two spots of small negative and positive flux. From a theoretical point of view, G_θ can be divided into three contributions: the motion of IP with regard to OP, ON, and IN. Figure 5 of Pariat *et al.* (2006) and Figure 6 of Pariat, Démoulin, and Nindos (2007) can be used to infer the resulting sign of helicity injection of these three contributions. The motion of IP with regard to the outer dipole is a shearing motion and injects positive helicity. The motion of IP with regard to the IN injects some negative helicity flux. However, IP and IN are almost aligned with the direction of the translational motion. Hence, the associated shearing is much weaker than that of IP with regard to the outer dipole. The resulting helicity flux is therefore much weaker. The summation of these three contributions explains the observed features in the G_θ map. The associated G_Φ map only exhibits positive helicity flux signal. In particular, it shows that helicity is also injected in the QSL connected to IP (see Figures 15c and 15e), with a stronger flux at the edges of the QSL (for the same reason as in Section 7.3). It also presents some weak positive helicity injection that allows to slightly distinguish the QSL in the positive polarity.

The flux transport velocity field of the $\Phi = 150^\circ$ configuration implies a global shearing as for the $\Phi = 120^\circ$ case. The difference is that now, the inner dipole is more aligned with the outer dipole. Hence, as IP moves, the shearing of the inner dipole is more negative than for $\Phi = 120^\circ$. Therefore, the total helicity flux distribution in IP is a sum of positive — from shearing with ON and OP — and negative — from shearing with IN — fluxes. This explains the resulting G_θ map (Figure 15b). On the other hand, G_Φ map presents mainly positive helicity injection (Figure 15d). In particular, a strong positive helicity injection is present in both external parts of the QSLs (Figures 15d and 15f). In the inner part, where IP and IN are magnetically connected, negative helicity injection is present. Such a result is actually expected since the white magnetic field lines of Figure 2f are sheared oppositely to the other magnetic field lines as IP translates towards the $y > 0$.

Note that, for the G_Φ maps considered in both nearly rigid rotation and translation of IP, for 43% of the photospheric mesh footpoints, the field lines

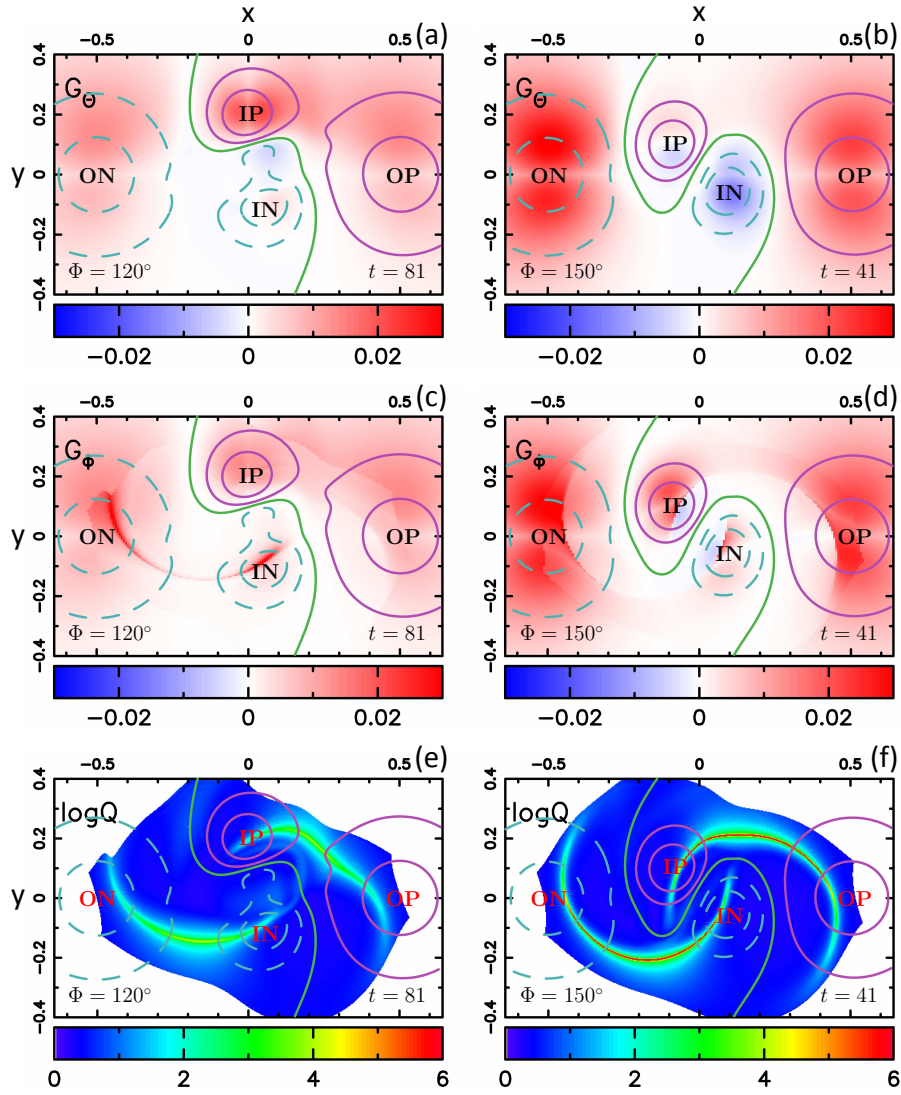


Figure 15. Results of two MHD simulations with a nearly solid translation of the inner magnetic polarity (IP) and nearly no motion in other polarities. The angle between the inner and outer bipoles at $t = 0$ is $\Phi = 120^\circ$ (left column) and $\Phi = 150^\circ$ (right column) and the simulation time is $t = 81$ and $t = 41$ Alfvén times respectively. The panels show the photospheric distribution of: (a,b) G_θ , (c,d) G_ϕ , and (e,f) $\log_{10} Q$. The drawing convention is the same as in Figure 14.

integration did not lead to a second footpoint on the $z = 0$ -plane (open-like magnetic field lines reaching the boundary of the mesh). Therefore, for these 43% photospheric footpoints — localized at the white regions of the squashing degree maps — the helicity flux density G_ϕ is set equal to G_θ . This is observable in the G_ϕ map of the translation model (Figure 15c), where we can identify an abrupt change of G_ϕ at the limit of white and blue regions of Figure 15e. In

order to compute G_{Φ} in a more extended part of the outer polarities, a larger numerical box is needed in the numerical simulations.

7.5. Errors Estimation

For both Φ configurations and both flux transport velocity fields, we compute the total helicity flux computed from G_{θ} and G_{Φ} for all simulations output files as a function of time. We then estimate the errors on the total helicity flux computed from G_{Φ} compared to G_{θ} by computing the rms of the difference of total fluxes. We find that the rms is $\approx 10^{-7} - 10^{-6}$ while the values of this total flux are $\approx 10^{-4} - 10^{-3}$. Although the total helicity fluxes computed from both helicity flux densities are mathematically strictly equal, numerically we find tiny differences due to the precision in G_{Φ} computation (see Equation (20)). However, they are typically $\approx 10^3$ times smaller than the typical values of the total helicity flux.

8. Conclusions

In this paper, we focus on the study of the flux of magnetic helicity through the photosphere. As magnetic helicity is a global 3D quantity, a density of magnetic helicity flux is only meaningful when defined by elementary magnetic flux tubes (Pariat, Démoulin, and Berger, 2005).

Our aim is to present the first implementation of a method that computes the helicity flux density at the photosphere by taking into account the magnetic field connectivity. In order to test our method and use it in future observational studies, we have performed a comparative analysis of the distribution of helicity injection at the photosphere using two proxies of helicity flux density: G_{θ} and G_{Φ} . We have analyzed their properties on simplified solar configurations considering analytical, extrapolated magnetic fields and fields from numerical simulations.

We find that, while the total helicity flux remains the same using G_{θ} or G_{Φ} , the distribution of helicity flux, however, can be significantly different. Using several test-cases, we confirm that G_{θ} does not always reveal the true distribution of helicity flux while G_{Φ} properly localizes the true site(s) of helicity injection. In particular, we show that G_{θ} can hide subtle variation of mutual helicity between neighboring field lines in a flux tube (*cf.* Sections 5 and 6). We also analyze the effect of strong connectivity gradients on the helicity distribution in systems containing QSLs. The error estimations highlight that our method of computing the field lines connectivity is very accurate using analytical and extrapolated magnetic fields as well as for magnetic fields from numerical simulations.

We finally discuss that some differences between G_{θ} and G_{Φ} maps are related to the underlying assumptions of field lines connectivity. G_{θ} provides the locally injected helicity flux when the injection timescale is much shorter than the transit Alfvén time between field line footpoints. G_{Φ} assumes that both magnetic field line footpoints are “aware” of the evolution of one another, hence, that the injection timescale is longer than the transit Alfvén time which is typically the case in most solar applications.

The use of the method that we have presented here will be quite useful when applied to actual observed ARs. For ARs with helicity flux density maps of uniform sign, while not changing the uniform character of the helicity injection, G_Φ will enable to more precisely localize the regions where magnetic helicity is injected and accumulated. For ARs displaying mixed signs of helicity in G_θ maps (Chandra *et al.*, 2010; Romano *et al.*, 2011; Romano and Zuccarello, 2011; Jing *et al.*, 2012), G_Φ will permit to remove the spurious mixed signal, displaying the true helicity flux distribution. It may result in a more complex and subtle injection of helicity, revealing mutual helicity changes between magnetic flux tubes, as in some examples presented in this study. G_Φ will allow to more strictly determine which ARs present injection of opposite sign of magnetic helicity and relate this pattern to their eruptivity (*e.g.*, Romano and Zuccarello, 2011). The G_Φ maps will enable to observationally test the theoretical hypothesis that more energy is eventually released when magnetic helicity annihilation occurs (Kusano, Suzuki, and Nishikawa, 1995; Linton, Dahlburg, and Antiochos, 2001). They will also allow to observationally test models based on magnetic helicity cancellation (Kusano *et al.*, 2002, 2004a).

Overall, G_Φ will enable us to truthfully track the injection of helicity into the solar corona, helping us to better understand the role of magnetic helicity in solar activity.

Acknowledgements The authors thank A. Canou for providing the potential and linear force-free fields computed with the XTRAPOL numerical code developed by T. Amari and supported by the Centre National d’Etudes Spatiales & the Ecole Polytechnique. The authors thank the referee for helpful comments that improved the clarity of the paper.

Appendix

A. Analytical Solutions for G_θ

In the following, we use the same notation as defined in Section 3. The flux transport velocity fields are given by Equations (11) – (15). The total magnetic flux in the positive (resp. negative) polarity is called Φ_+ (resp. $-\Phi_-$, with $\Phi_\pm > 0$). For generality purpose, Φ_- can be different from Φ_+ , and no specific assumption is made concerning the magnetic field configuration.

A.1. Two Separating Magnetic Polarities

We consider two opposite magnetic polarities separating in the x -direction at constant speed and without any rotation. The flux transport velocity field is given by Equation (11). Because the velocity field is constant in each polarity, the terms of Equation (4) associated to (M, M') in the same polarity are zero as a consequence of $\mathbf{u}' = \mathbf{u}$.

In this case, we have $\mathbf{u} - \mathbf{u}' = \mp 2U_0 \mathbf{e}_x$ when $\pm B_n(M) > 0$ and $\mp B_n(M') > 0$, which leads to:

$$\mathbf{M}' \mathbf{M} \times (\mathbf{u} - \mathbf{u}')|_n = \pm 2U_0 \mathbf{M}' \mathbf{M} \cdot \mathbf{e}_y. \quad (25)$$

Thus, Equation (4) leads to:

$$G_\theta(M(\mathbf{x})) = \mp \frac{U_0 B_n}{\pi} \left(\int_{M' \text{ in } P_\mp} B'_n \frac{\mathbf{M}' \mathbf{M}}{|\mathbf{M}' \mathbf{M}|^2} d\mathcal{S}' \right) \cdot \mathbf{e}_y, \text{ for } \pm B_n(M) > 0. \quad (26)$$

This integral can be computed by analogy to the electric field created by a 2D distribution of charge, $\sigma(M) = B'_n(M)$, of an infinite cylinder of radius R (of vertical axis crossing the $z = 0$ plane at point O_\mp), using Gauss theorem, *i.e.*, :

$$\int_{M' \text{ in } P_\mp} B'_n \frac{\mathbf{M}' \mathbf{M}}{|\mathbf{M}' \mathbf{M}|^2} d\mathcal{S}' = \mp \frac{\mathbf{O}_\mp \mathbf{M}}{|\mathbf{O}_\mp \mathbf{M}|^2} \Phi_\mp. \quad (27)$$

Hence, we find that the helicity flux density is given by Equation (12).

A.2. One Polarity Rigidly Rotating Around the Other

In this model, the negative polarity rigidly rotates around the positive one. The velocity field is given by Equation (13). There are four cases to consider.

· c1. If $B_n(M) > 0$ and $B_n(M') > 0$, then $\mathbf{u} - \mathbf{u}' = 0$ and the associated term of Equation (4) is null.

· c2. If $B_n(M) > 0$ and $B_n(M') < 0$, then $\mathbf{u} - \mathbf{u}' = -\Omega \mathbf{e}_z \times \mathbf{O}_+ \mathbf{M}'$ and:

$$\mathbf{M}' \mathbf{M} \times (\mathbf{u} - \mathbf{u}')|_n = -(\mathbf{M}' \mathbf{M} \cdot \mathbf{O}_+ \mathbf{M}') \Omega. \quad (28)$$

The helicity flux density is then (using $\mathbf{O}_+ \mathbf{M}' = \mathbf{O}_+ \mathbf{M} - \mathbf{M}' \mathbf{M}$):

$$\begin{aligned} G_\theta(M(\mathbf{x})) &= \frac{\Omega B_n}{2\pi} \int_{M' \text{ in } P_-} B'_n \left(\frac{\mathbf{O}_+ \mathbf{M} \cdot \mathbf{M}' \mathbf{M}}{|\mathbf{M}' \mathbf{M}|^2} - 1 \right) d\mathcal{S}' \\ &= \frac{\Omega B_n}{2\pi} \left(\mathbf{O}_+ \mathbf{M} \cdot \int_{M' \text{ in } P_-} B'_n \frac{\mathbf{M}' \mathbf{M}}{|\mathbf{M}' \mathbf{M}|^2} d\mathcal{S}' + \Phi_- \right) \\ &= \frac{\Omega B_n}{2\pi} \left(- \frac{\mathbf{O}_+ \mathbf{M} \cdot \mathbf{O}_- \mathbf{M}}{|\mathbf{O}_- \mathbf{M}|^2} \Phi_- + \Phi_- \right), \text{ for } B_n(M) > 0, \end{aligned} \quad (29)$$

which, by regrouping terms, leads to Equation (14).

· c3. If $B_n(M) < 0$ and $B_n(M') > 0$, then $\mathbf{u} - \mathbf{u}' = \Omega \mathbf{e}_z \times \mathbf{O}_+ \mathbf{M}$ and:

$$\mathbf{M}' \mathbf{M} \times (\mathbf{u} - \mathbf{u}')|_n = (\mathbf{M}' \mathbf{M} \cdot \mathbf{O}_+ \mathbf{M}) \Omega, \quad (30)$$

which, using Equation (27) leads to:

$$G_\theta(M(\mathbf{x})) = - \frac{\Omega B_n}{2\pi} \Phi_+, \text{ for } (B_n(M) < 0, B_n(M') > 0). \quad (31)$$

· c4. If $B_n(M) < 0$ and $B_n(M') < 0$, $\mathbf{u} - \mathbf{u}' = \Omega \mathbf{e}_z \times \mathbf{M}' \mathbf{M}$ and:

$$\mathbf{M}' \mathbf{M} \times (\mathbf{u} - \mathbf{u}')|_n = |\mathbf{M}' \mathbf{M}|^2 \Omega, \quad (32)$$

leading to:

$$G_\theta(M(\mathbf{x})) = \frac{\Omega B_n}{2\pi} \Phi_-, \text{ for } (B_n(M) < 0, B_n(M') < 0). \quad (33)$$

Then the total helicity flux density within the region $B_n(M) < 0$ is therefore:

$$G_\theta(M(\mathbf{x})) = -\frac{\Omega B_n}{2\pi} (\Phi_+ - \Phi_-), \text{ for } B_n(M) < 0. \quad (34)$$

Note that, in the particular case of two magnetic-flux balanced polarities, $\Phi_+ = \Phi_-$ and $G_\theta = 0$ for $B_n(M) < 0$.

A.3. Two Counter-rotating Magnetic Polarities

In this model, the positive polarity rotates clockwise around its center, while the negative rotates counterclockwise around its center. The velocity field is given by Equation (15). There are four cases to consider, which, by symmetry, reduce to two cases.

· c1. If $B_n(M) > 0$ and $B_n(M') > 0$, we have $\mathbf{u} - \mathbf{u}' = -\Omega \mathbf{e}_z \times \mathbf{M}'\mathbf{M}$, which leads to:

$$\mathbf{M}'\mathbf{M} \times (\mathbf{u} - \mathbf{u}')|_n = -|\mathbf{M}'\mathbf{M}|^2 \Omega, \quad (35)$$

giving:

$$G_\theta(M(\mathbf{x})) = \frac{\Omega B_n}{2\pi} \Phi_+, \text{ for } (B_n(M) > 0, B_n(M') > 0). \quad (36)$$

· c2. If $B_n(M) > 0$ and $B_n(M') < 0$, we have $\mathbf{u} - \mathbf{u}' = \Omega \mathbf{e}_z \times (\mathbf{M}'\mathbf{M} - \mathbf{O}_+\mathbf{M} - \mathbf{O}_-\mathbf{M})$, which leads to:

$$\mathbf{M}'\mathbf{M} \times (\mathbf{u} - \mathbf{u}')|_n = |\mathbf{M}'\mathbf{M}|^2 \Omega - (\mathbf{M}'\mathbf{M} \cdot (\mathbf{O}_+\mathbf{M} + \mathbf{O}_-\mathbf{M})) \Omega, \quad (37)$$

giving (using $\mathbf{O}_+\mathbf{M} = \mathbf{O}_+\mathbf{O}_- + \mathbf{O}_-\mathbf{M}$):

$$\begin{aligned} G_\theta(M(\mathbf{x})) &= -\frac{\Omega B_n}{2\pi} \int_{M' \text{ in } P_-} B'_n \left(1 - \frac{(\mathbf{O}_+\mathbf{O}_- + 2 \mathbf{O}_-\mathbf{M}) \cdot \mathbf{M}'\mathbf{M}}{|\mathbf{M}'\mathbf{M}|^2} \right) dS' \\ &= \frac{\Omega B_n}{2\pi} \left(\Phi_- + (\mathbf{O}_+\mathbf{O}_- + 2 \mathbf{O}_-\mathbf{M}) \cdot \int_{M' \text{ in } P_-} B'_n \frac{\mathbf{M}'\mathbf{M}}{|\mathbf{M}'\mathbf{M}|^2} dS' \right) \\ &= \frac{\Omega B_n}{2\pi} \left(\Phi_- - \frac{(\mathbf{O}_+\mathbf{O}_- + 2 \mathbf{O}_-\mathbf{M}) \cdot \mathbf{O}_-\mathbf{M}}{|\mathbf{O}_-\mathbf{M}|^2} \Phi_- \right) \\ &= -\frac{\Omega B_n \Phi_-}{2\pi} \left(1 + \frac{\mathbf{O}_-\mathbf{M} \cdot \mathbf{O}_+\mathbf{O}_-}{|\mathbf{O}_-\mathbf{M}|^2} \right), \end{aligned} \quad (38)$$

for $(B_n(M) > 0, B_n(M') < 0)$.

The total helicity flux density in the positive polarity is obtained by summing

Equation (36) and Equation (38) and supposing $\Phi_+ = \Phi_- = \Phi_0$ to simplify:

$$G_\theta(M(\mathbf{x})) = -\frac{\Omega B_n}{2\pi} \frac{\mathbf{O}_- \mathbf{M} \cdot \mathbf{O}_+ \mathbf{O}_-}{|\mathbf{O}_- \mathbf{M}|^2} \Phi_0, \text{ for } B_n(M) > 0. \quad (39)$$

Following the same derivation as above for $B_n(M) < 0$, we find Equation (16).

References

- Amari, T., Aly, J.-J.: 2010, Observational constraints on well-posed reconstruction methods and the optimization-Grad-Rubin method. *Astron. Astrophys.* **522**, A52. doi:10.1051/0004-6361/200913058.
- Amari, T., Boulmezaoud, T.Z., Aly, J.J.: 2006, Well posed reconstruction of the solar coronal magnetic field. *Astron. Astrophys.* **446**, 691–705. doi:10.1051/0004-6361:20054076.
- Amari, T., Boulmezaoud, T.Z., Mikic, Z.: 1999, An iterative method for the reconstruction of the solar coronal magnetic field. I. Method for regular solutions. *Astron. Astrophys.* **350**, 1051–1059.
- Aulanier, G., Pariat, E., Démoulin, P.: 2005, Current sheet formation in quasi-separatrix layers and hyperbolic flux tubes. *Astron. Astrophys.* **444**, 961–976. doi:10.1051/0004-6361:20053600.
- Bagalá, L.G., Mandrini, C.H., Rovira, M.G., Démoulin, P.: 2000, Magnetic reconnection: a common origin for flares and AR interconnecting arcs. *Astron. Astrophys.* **363**, 779–788.
- Baker, D., van Driel-Gesztelyi, L., Mandrini, C.H., Démoulin, P., Murray, M.J.: 2009, Magnetic reconnection along quasi-separatrix layers as a driver of ubiquitous active region outflows. *Astrophys. J.* **705**, 926–935. doi:10.1088/0004-637X/705/1/926.
- Berger, M.A.: 2003, Topological quantities in magnetohydrodynamics. In: Ferriz-Mas, A., Núñez, M. (eds.) *Advances in Nonlinear Dynamics*, Taylor and Francis Group, London, 345–383.
- Berger, M.A.: 1984, Rigorous new limits on magnetic helicity dissipation in the solar corona. *Geophys. Astrophys. Fluid Dyn.* **30**, 79–104. doi:10.1080/03091928408210078.
- Chae, J.: 2007, Measurements of magnetic helicity injected through the solar photosphere. *Adv. Space Res.* **39**, 1700–1705. doi:10.1016/j.asr.2007.01.035.
- Chae, J.: 2001, Observational determination of the rate of magnetic helicity transport through the solar surface via the horizontal motion of field line footpoints. *Astrophys. J. Lett.* **560**, L95–L98. doi:10.1086/324173.
- Chae, J., Moon, Y.-J., Park, Y.-D.: 2004, Determination of magnetic helicity content of solar active regions from SOHO/MDI magnetograms. *Solar Phys.* **223**, 39–55. doi:10.1007/s11207-004-0938-9.
- Chandra, R., Pariat, E., Schmieder, B., Mandrini, C.H., Uddin, W.: 2010, How can a negative magnetic helicity active region generate a positive helicity magnetic cloud? *Solar Phys.* **261**, 127–148. doi:10.1007/s11207-009-9470-2.
- Démoulin, P.: 2006, Extending the concept of separatrices to QSLs for magnetic reconnection. *Adv. Space Res.* **37**, 1269–1282. doi:10.1016/j.asr.2005.03.085.
- Démoulin, P., Pariat, E.: 2009, Modelling and observations of photospheric magnetic helicity. *Adv. Space Res.* **43**, 1013–1031. doi:10.1016/j.asr.2008.12.004.
- Démoulin, P., Pariat, E., Berger, M.A.: 2006, Basic properties of mutual magnetic helicity. *Solar Phys.* **233**, 3–27. doi:10.1007/s11207-006-0010-z.
- Démoulin, P., Priest, E.R., Lonie, D.P.: 1996, Three-dimensional magnetic reconnection without null points 2. Application to twisted flux tubes. *J. Geophys. Res.* **101**, 7631–7646. doi:10.1029/95JA03558.
- Démoulin, P., Bagalá, L.G., Mandrini, C.H., Henoux, J.C., Rovira, M.G.: 1997, Quasi-separatrix layers in solar flares. II. Observed magnetic configurations. *Astron. Astrophys.* **325**, 305–317.
- Démoulin, P., Mandrini, C.H., van Driel-Gesztelyi, L., Thompson, B.J., Plunkett, S., Kovári, Z., Aulanier, G., Young, A.: 2002, What is the source of the magnetic helicity shed by CMEs? The long-term helicity budget of AR 7978. *Astron. Astrophys.* **382**, 650–665. doi:10.1051/0004-6361:20011634.

- Démoulin, P.: 2007, Recent theoretical and observational developments in magnetic helicity studies. *Adv. Space Res.* **39**, 1674–1693. doi:10.1016/j.asr.2006.12.037.
- Démoulin, P., Berger, M.A.: 2003, Magnetic energy and helicity fluxes at the photospheric level. *Solar Phys.* **215**, 203–215. doi:10.1023/A:1025679813955.
- DeVore, C.R.: 2000, Magnetic helicity generation by solar differential rotation. *Astrophys. J.* **539**, 944–953. doi:10.1086/309274.
- Emonet, T., Moreno-Insertis, F.: 1998, The physics of twisted magnetic tubes rising in a stratified medium: Two-dimensional results. *Astrophys. J.* **492**, 804–821. doi:10.1086/305074.
- Finn, J.M., Antonsen, J. T. M.: 1985, Magnetic helicity: What is it and what is it good for? *Comments Plasma Phys. Controlled Fusion* **9**, 111–120.
- Georgoulis, M.K., Rust, D.M., Pevtsov, A.A., Bernasconi, P.N., Kuzanyan, K.M.: 2009, Solar magnetic helicity injected into the heliosphere: Magnitude, balance, and periodicities over solar cycle 23. *Astrophys. J. Lett.* **705**, L48–L52. doi:10.1088/0004-637X/705/1/L48.
- Green, L.M., López Fuentes, M.C., Mandrini, C.H., van Driel-Gesztelyi, L., Démoulin, P.: 2002a, Long-term helicity evolution in NOAA active region 8100. In: Sawaya-Lacoste, H. (ed.) *SOLSPA 2001, Proceedings of the Second Solar Cycle and Space Weather Euroconference, ESA SP-477*, 43–46.
- Green, L.M., López fuentes, M.C., Mandrini, C.H., Démoulin, P., Van Driel-Gesztelyi, L., Culhane, J.L.: 2002b, The magnetic helicity budget of a CME-prolific active region. *Solar Phys.* **208**, 43–68. doi:10.1023/A:1019658520033.
- Jeong, H., Chae, J.: 2007, Magnetic helicity injection in active regions. *Astrophys. J.* **671**, 1022–1033. doi:10.1086/522666.
- Jing, J., Park, S.-H., Liu, C., Lee, J., Wiegmann, T., Xu, Y., Deng, N., Wang, H.: 2012, Evolution of relative magnetic helicity and current helicity in NOAA active region 11158. *Astrophys. J. Lett.* **752**, L9. doi:10.1088/2041-8205/752/1/L9.
- Kazachenko, M.D., Canfield, R.C., Longcope, D.W., Qiu, J.: 2012, Predictions of energy and helicity in four major eruptive solar flares. *Solar Phys.* **277**, 165–183. doi:10.1007/s11207-011-9786-6.
- Kusano, K., Suzuki, Y., Nishikawa, K.: 1995, A solar flare triggering mechanism based on the Woltjer-Taylor minimum energy principle. *Astrophys. J.* **441**, 942–951. doi:10.1086/175413.
- Kusano, K., Maeshiro, T., Yokoyama, T., Sakurai, T.: 2004a, The trigger mechanism of solar flares in a coronal arcade with reversed magnetic shear. *Astrophys. J.* **610**, 537–549. doi:10.1086/421547.
- Kusano, K., Maeshiro, T., Yokoyama, T., Sakurai, T.: 2002, Measurement of magnetic helicity injection and free energy loading into the solar corona. *Astrophys. J.* **577**, 501–512. doi:10.1086/342171.
- Kusano, K., Maeshiro, T., Yokoyama, T., Sakurai, T.: 2004b, Study of magnetic helicity in the solar corona. In: Sakurai, T., Sekii (eds.) *The Solar-B Mission and the Forefront of Solar Physics, ASP Conf. Ser.* **325**, 175–184.
- LaBonte, B.J., Georgoulis, M.K., Rust, D.M.: 2007, Survey of magnetic helicity injection in regions producing X-class flares. *Astrophys. J.* **671**, 955–963. doi:10.1086/522682.
- Linton, M.G., Antiochos, S.K.: 2002, Theoretical energy analysis of reconnecting twisted magnetic flux tubes. *Astrophys. J.* **581**, 703–717. doi:10.1086/344218.
- Linton, M.G., Antiochos, S.K.: 2005, Magnetic flux tube reconnection: Tunneling versus slingshot. *Astrophys. J.* **625**, 506–521. doi:10.1086/429585.
- Linton, M.G., Dahlburg, R.B., Antiochos, S.K.: 2001, Reconnection of twisted flux tubes as a function of contact angle. *Astrophys. J.* **553**, 905–921. doi:10.1086/320974.
- Longcope, D.W.: 2004, Inferring a photospheric velocity field from a sequence of vector magnetograms: The minimum energy fit. *Astrophys. J.* **612**, 1181–1192. doi:10.1086/422579.
- Longcope, D.W., Pevtsov, A.A.: 2003, Helicity transport and generation in the solar convection zone. *Adv. Space Res.* **32**, 1845–1853. doi:10.1016/S0273-1177(03)90618-1.
- Low, B.C.: 1997, The role of coronal mass ejections in solar activity. In: Crooker, N., Joselyn, J.A., Feynman, J. (eds.) *Coronal Mass Ejections, AGU Geophys. Monogr* **99**, 39–48. doi:10.1029/GM099p0039.
- Luoni, M.L., Démoulin, P., Mandrini, C.H., van Driel-Gesztelyi, L.: 2011, Twisted flux tube emergence evidenced in longitudinal magnetograms: Magnetic tongues. *Solar Phys.* **270**, 45–74. doi:10.1007/s11207-011-9731-8.
- Mandrini, C.H., Démoulin, P., Bagala, L.G., van Driel-Gesztelyi, L., Henoux, J.C., Schmieder, B., Rovira, M.G.: 1997, Evidence of magnetic reconnection from $H\alpha$,

- soft X-ray and photospheric magnetic field observations. *Solar Phys.* **174**, 229–240. doi:10.1023/A:1004950009970.
- Mandrini, C.H., Démoulin, P., van Driel-Gesztelyi, L., van Driel-Gesztelyi, L., van Driel-Gesztelyi, L., van Driel-Gesztelyi, L.L.M., López Fuentes, M.C.: 2004, Magnetic helicity budget of solar-active regions from the photosphere to magnetic clouds. *Astrophys. Space Sci.* **290**, 319–344. doi:10.1023/B:ASTR.0000032533.31817.0e.
- Mandrini, C.H., Démoulin, P., Schmieder, B., Deluca, E.E., Pariat, E., Uddin, W.: 2006, Companion event and precursor of the X17 flare on 28 October 2003. *Solar Phys.* **238**, 293–312. doi:10.1007/s11207-006-0205-3.
- Masson, S., Pariat, E., Aulanier, G., Schrijver, C.J.: 2009, The nature of flare ribbons in coronal null-point topology. *Astrophys. J.* **700**, 559–578. doi:10.1088/0004-637X/700/1/559.
- Moon, Y.-J., Chae, J., Choe, G.S., Wang, H., Park, Y.D., Yun, H.S., Yurchyshyn, V., Goode, P.R.: 2002, Flare activity and magnetic helicity injection by photospheric horizontal motions. *Astrophys. J.* **574**, 1066–1073. doi:10.1086/340975.
- Nindos, A., Zhang, J., Zhang, H.: 2003, The magnetic helicity budget of solar active regions and coronal mass ejections. *Astrophys. J.* **594**, 1033–1048. doi:10.1086/377126.
- Pariat, E., Démoulin, P., Berger, M.A.: 2005, Photospheric flux density of magnetic helicity. *Astron. Astrophys.* **439**, 1191–1203. doi:10.1051/0004-6361:20052663.
- Pariat, E., Démoulin, P., Nindos, A.: 2007, How to improve the maps of magnetic helicity injection in active regions? *Adv. Space Res.* **39**, 1706–1714. doi:10.1016/j.asr.2007.02.047.
- Pariat, E., Nindos, A., Démoulin, P., Berger, M.A.: 2006, What is the spatial distribution of magnetic helicity injected in a solar active region? *Astron. Astrophys.* **452**, 623–630. doi:10.1051/0004-6361:20054643.
- Pevtsov, A.A., Canfield, R.C., Metcalf, T.R.: 1995, Latitudinal variation of helicity of photospheric magnetic fields. *Astrophys. J. Lett.* **440**, L109–L112. doi:10.1086/187773.
- Romano, P., Zuccarello, F.: 2011, Flare occurrence and the spatial distribution of the magnetic helicity flux. *Astron. Astrophys.* **535**, A1. doi:10.1051/0004-6361/201117594.
- Romano, P., Pariat, E., Sicari, M., Zuccarello, F.: 2011, A solar eruption triggered by the interaction between two magnetic flux systems with opposite magnetic helicity. *Astron. Astrophys.* **525**, A13. doi:10.1051/0004-6361/201014437.
- Rust, D.M.: 1994, Spawning and shedding helical magnetic fields in the solar atmosphere. *Geophys. Res. Lett.* **21**, 241–244. doi:10.1029/94GL00003.
- Savcheva, A., Pariat, E., van Ballegoijen, A., Aulanier, G., DeLuca, E.: 2012, Sigmoidal active region on the Sun: Comparison of a magnetohydrodynamical simulation and a nonlinear force-free field model. *Astrophys. J.* **750**, 15. doi:10.1088/0004-637X/750/1/15.
- Schuck, P.W.: 2005, Local correlation tracking and the magnetic induction equation. *Astrophys. J. Lett.* **632**, L53–L56. doi:10.1086/497633.
- Schuck, P.W.: 2006, Tracking magnetic footpoints with the magnetic induction equation. *Astrophys. J.* **646**, 1358–1391. doi:10.1086/505015.
- Schuck, P.W.: 2008, Tracking vector magnetograms with the magnetic induction equation. *Astrophys. J.* **683**, 1134–1152. doi:10.1086/589434.
- Taylor, J.B.: 1974, Relaxation of toroidal plasma and generation of reverse magnetic fields. *Phys. Rev. Lett.* **33**, 1139–1141. doi:10.1103/PhysRevLett.33.1139.
- Titov, V.S., Hornig, G., Démoulin, P.: 2002, Theory of magnetic connectivity in the solar corona. *J. Geophys. Res.* **107**, 1164. doi:10.1029/2001JA000278.
- Valori, G., Démoulin, P., Pariat, E.: 2012, Comparing values of the relative magnetic helicity in finite volumes. *Solar Phys.* **278**, 347–366. doi:10.1007/s11207-012-9951-6.
- van Driel-Gesztelyi, L., Mandrini, C.H., Thompson, B., Plunkett, S., Aulanier, G., Démoulin, P., Schmieder, B., de Forest, C.: 1999, Long-term magnetic evolution of an AR and its CME activity. In: Schmieder, B., Hofmann, A., Staude, J. (eds.) *Third Advances in Solar Physics Euroconference: Magnetic Fields and Oscillations, ASP Conf. Ser.* **184**, 302–306.
- Welsch, B.T., Fisher, G.H., Abbett, W.P., Regnier, S.: 2004, ILCT: Recovering photospheric velocities from magnetograms by combining the induction equation with local correlation tracking. *Astrophys. J.* **610**, 1148–1156. doi:10.1086/421767.
- Welsch, B.T., Abbett, W.P., De Rosa, M.L., Fisher, G.H., Georgoulis, M.K., Kusano, K., Longcope, D.W., Ravindra, B., Schuck, P.W.: 2007, Tests and comparisons of velocity-inversion techniques. *Astrophys. J.* **670**, 1434–1452. doi:10.1086/522422.
- Welsch, B.T., Li, Y., Schuck, P.W., Fisher, G.H.: 2009, What is the relationship between photospheric flow fields and solar flares? *Astrophys. J.* **705**, 821–843. doi:10.1088/0004-637X/705/1/821.

-
- Yamada, M.: 1999, Study of magnetic helicity and relaxation phenomena in laboratory plasmas. In: Brown, M.R., Canfield, R.C., Pevtsov, A.A. (eds.) *Magnetic Helicity in Space and Laboratory Plasmas*, *AGU Geophys. Monogr.* **11**, 129–140. doi:10.1029/GM111p0129.
- Yamamoto, T.T., Kusano, K., Maeshiro, T., Yokoyama, T., Sakurai, T.: 2005, Magnetic helicity injection and sigmoidal coronal loops. *Astrophys. J.* **624**, 1072–1079. doi:10.1086/429363.
- Yang, S., Zhang, H.: 2012, Large-scale magnetic helicity fluxes estimated from MDI magnetic synoptic charts over the solar cycle 23. *Astrophys. J.* **758**, 61. doi:10.1088/0004-637X/758/1/61.
- Zhang, M., Flyer, N.: 2008, The dependence of the helicity bound of force-free magnetic fields on boundary conditions. *Astrophys. J.* **683**, 1160–1167. doi:10.1086/589993.
- Zhang, M., Flyer, N., Low, B.C.: 2006, Magnetic field confinement in the corona: The role of magnetic helicity accumulation. *Astrophys. J.* **644**, 575–586. doi:10.1086/503353.
- Zhang, M., Flyer, N., Low, B.C.: 2012, Magnetic helicity of self-similar axisymmetric force-free fields. *Astrophys. J.* **755**, 78. doi:10.1088/0004-637X/755/1/78.